

DESIGN OF SYNTHETIC JET ACTUATOR FOR FLIGHT CONTROL OF
SMALL UAV

A Thesis

Submitted to the Faculty

of

Embry-Riddle Aeronautical University

by

Priyanka Pagadala

In Partial Fulfillment of the

Requirements for the Degree

of

Master of Science in Aerospace Engineering

June 2015

Embry-Riddle Aeronautical University

Daytona Beach, Florida

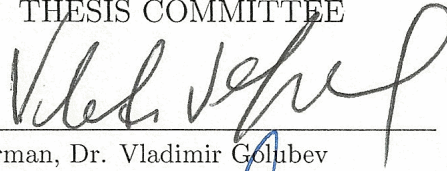
DESIGN OF SYNTHETIC JET ACTUATOR FOR FLIGHT CONTROL OF
SMALL UAV

by

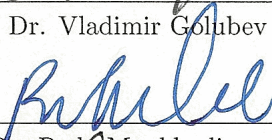
Priyanka Pagadala

A Thesis prepared under the direction of the candidate's committee chairman, Dr. Vladimir Golubev, Department of Aerospace Engineering, and has been approved by the members of the thesis committee. It was submitted to the School of Graduate Studies and Research and was accepted in partial fulfillment of the requirements for the degree of Master of Science in Aerospace Engineering.

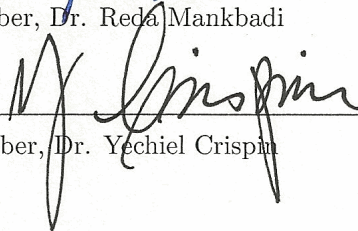
THESIS COMMITTEE



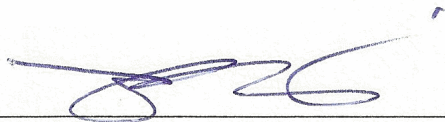
Chairman, Dr. Vladimir Golubev



Member, Dr. Reda Mankbadi



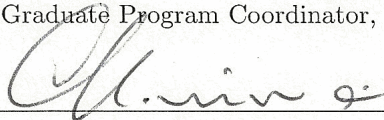
Member, Dr. Yechiel Crispin



Department Chair, Dr. Anastasios Lyrintzis
or Graduate Program Coordinator, Dr. Yi Zhao

7/16/2015

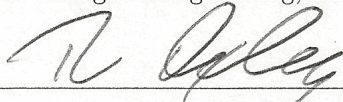
Date



Dean of College of Engineering, Dr. Maj Mirmirani

7/16/2015

Date



Associate VP for Academics, Dr. Robert Oxley

7/20/2015

Date

ACKNOWLEDGMENTS

I would like to thank my adviser, Dr. Vladimir Golubev, for his financial support, motivation, and his contributions throughout the project. I would like to thank Dr. Reda Mankbadi for being inspirational and for giving me some insights on physics of flows. I would like to acknowledge the members of the brown bag research group Lap, Sanjay, Sam, and Marco for their support that helped with my research.

Special Thanks to Michael Reed for mathematical insights, resolving mesh related issues, and for his support. Thank you to Dr. Yechiel Crispin and Dr. Anastasios Lyrintzis for their valuable suggestions in improving the project. I would also like to thank Bill Russo for helping to fabricate actuator models for the experiment.

Finally, I would like to Thank my family and friends who supported and believed in me to pursue my interests.

TABLE OF CONTENTS

	Page
LIST OF TABLES	vi
LIST OF FIGURES	vii
SYMBOLS	ix
ABBREVIATIONS	xi
ABSTRACT	xii
1 Flow Control using Synthetic Jets	1
1.1 Evolution of Flow Control	1
1.1.1 Passive Flow Control	2
1.1.2 Active Flow Control	3
1.1.3 Reactive Control Loops	3
1.1.4 Applied AFC Device	5
1.2 Synthetic Jet Actuators	6
1.2.1 Literature Review	8
1.2.2 Current Research	10
2 Lumped Element Modeling	11
2.1 Gallas LEM	11
2.1.1 Assumptions	12
2.1.2 Circuit Details	13
2.1.3 Refined LEM	14
2.1.4 Orifice Physics	16
2.1.5 Results	20
2.2 Development of an Actuator	21
2.2.1 Actuator Geometry	21
2.2.2 Diaphragm Boundary	22
2.2.3 Prototype	23
3 Computational Fluid Dynamics	25
3.1 CAD Geometry and Meshing	25
3.1.1 Rectangular Slot	26
3.1.2 Circular Orifice	27
3.1.3 Mesh Independence	28
3.2 Numerical Solution	29
3.2.1 Turbulence Model	30

	Page
3.2.2 Boundary Conditions	31
3.2.3 Time Stepping	33
3.3 Results	34
4 Hot Wire Anemometry	37
4.1 Purpose	37
4.2 Equipment	38
4.3 Principles	38
4.4 Anemometer	40
4.5 Method	42
4.6 Results	45
4.7 Alternate Model	47
5 Wind Tunnel Experiment	51
5.1 Modified Glauert Airfoil	51
5.2 Strain Gauge Principle	52
5.3 Calibration	53
5.4 Operation of Wind Tunnel	55
5.5 Results	58
6 Conclusions	62
REFERENCES	64

LIST OF TABLES

Table	Page
2.1 Difference in shapes for orifice (equations)	19
2.2 Geometric parameters for actuators <i>Model-C</i> and <i>Model-R</i>	21
2.3 Selected piezoelectric diaphragm properties	22
4.1 Geometric parameters and properties of (de Luca, Girefoglio, & Coppola, 2000) actuator	48
4.2 Piezoelectric diaphragm properties and dimensions (de Luca et al., 2000)	48
5.1 Modified Glauert wing dimensions	51

LIST OF FIGURES

Figure	Page
1.1 Flow control strategies (Gad-El-Hak, 2000)	4
1.2 Inflow and outflow vortex generation (Mohseni & Mittal, 2014)	6
1.3 Formation of synthetic jets based on the Reynolds number (Holman, 2006)	7
2.1 LEM λ_δ assumption (Mohseni & Mittal, 2014)	12
2.2 Circuit representation components (Gallas, Sheplak, & Cattafesta, 2005)	13
2.3 Circuit representation impedances (Mohseni & Mittal, 2014)	14
2.4 Refined LEM technique to obtain $\{\omega_\delta, V_j\}$ frequency response plot for jet exit velocities (Gallas, Holman, & Cattafesta, 2005)	15
2.5 Comparison between control volume terms and the impedance of orifice (Gallas, Holman, & Cattafesta, 2005)	16
2.6 LEM result for <i>Model-C</i> $\{\omega_\delta, V_j\}$	20
2.7 LEM result for <i>Model-R</i> $\{\omega_\delta, V_j\}$	20
2.8 Clamped boundary (Mohseni & Mittal, 2014)	22
2.9 Pinned boundary (Mohseni & Mittal, 2014)	23
2.10 Circular orifice geometry in CATIA from <i>Model-C</i>	24
2.11 Circular orifice actuator, prototype <i>Model-C</i>	24
3.1 SJA and ambient domain geometry top view for <i>Model-R</i>	25
3.2 Meshed SJA with ambient air computational domain	26
3.3 Equiangle skewness in <i>Model-C</i> computational mesh	27
3.4 Construction lines for circular orifice	28
3.5 Velocity profile mesh independence comparison $\{d_O, V_j\}$	29
3.6 <i>Model-R</i> velocity profiles $\{d_O, V_j\}, \{w_O, V_j\}$	34
3.7 <i>Model-C</i> velocity profiles $\{d_O, V_j\}$	35
4.1 Hot wire anemometer circuit	39

Figure	Page
4.2 Hot wire probe	40
4.3 Anemometer with <i>Channel 1</i> connection	41
4.4 HWA interface board	41
4.5 Function generator E_δ with <i>Model-C</i> and <i>Model-R</i>	43
4.6 Experimental setup with function generator, amplifier, SJA, hot wire probe, anemometer, DAQ board, and computer	43
4.7 Hot wire probe and <i>Model-R</i> SJA with rectangular slot	44
4.8 Frequency response for <i>Model-C</i> LEM and HWA experiment $\{\omega_\delta, \bar{V}_j\}$.	45
4.9 Frequency response for <i>Model-R</i> LEM and HWA experiment $\{\omega_\delta, \bar{V}_j\}$.	45
4.10 Frequency response graph for actuators <i>Model -C, -R, and -D</i> $\{\omega_\delta, \bar{V}_j\}$	46
4.11 Numerical-experimental comparison of average exit flow velocity frequency response $\{\omega_\delta, \bar{V}_j\}$, (de Luca et al., 2000)	49
4.12 Experimental validation of actuator developed using LEM model based on Sharma's work vs Gallas LEM model using (de Luca et al., 2000) actuator design $\{\omega_\delta, V_j\}$	50
5.1 Modified Glauert airfoil	52
5.2 Lift component calibration	54
5.3 Wind tunnel with actuator setup	56
5.4 Experimental setup of the wing	57
5.5 Experimental setup of the wing with actuator embedded	57
5.6 Lift curve plot for clean and SJA case at 5 <i>m/s</i> $\{\alpha, C_L\}$	58
5.7 Lift curve plot for clean and SJA case at 10 <i>m/s</i> $\{\alpha, C_L\}$	59
5.8 Drag curve plots for clean and SJA case $\{\alpha, C_D\}$	60
5.9 Moment curve plots for clean and SJA case $\{\alpha, C_M\}$	61

SYMBOLS

d_O	Orifice/slot size
w_O	Width of slot
w_C	Width of cavity
h_N	Orifice neck height
h_C	Cavity height
l_C	Cavity length
A_O	Orifice area
A_D	Diaphragm/piston area
V_C	Cavity volume
t_D	Diaphragm component thickness
d_D	Diaphragm component diameter
b_w	Wing span
c_w	Airfoil chord
s_w	Surface area of the wing
x_{TE}	Distance from actuator to the trailing edge
δ	Diaphragm displacement function
δ_x	Peak to peak diaphragm displacement
T_δ	Period of diaphragm waveform
λ_δ	Wavelength of pressure oscillation
ω_δ	Diaphragm operating frequency
ω_D	Diaphragm fundamental mechanical frequency
ω_H	Helmholtz resonance acoustic frequency
E_δ	Voltage of diaphragm signal
V_j	Centerline jet velocity at orifice exit
\overline{V}_j	Spatially averaged exit velocity
∇_δ	Diaphragm volumetric displacement
Z_{aD}	Acoustic diaphragm impedance
Z_{aC}	Acoustic cavity impedance
Z_{aO}	Acoustic orifice impedance
Q_D	Diaphragm volumetric flow rate
Q_C	Cavity volumetric flow rate
Q_{out}	Orifice exit volumetric flow rate
Q_j	Computed volumetric flow rate
R_{aN}	Acoustic neck resistance, fully developed viscous flow
$R_{aO,l}$	Acoustic orifice linear resistance
$R_{aO,nl}$	Acoustic orifice nonlinear resistance
R_{aCf}	Acoustic resistance, developing viscous flow

M_{aN}	Acoustic neck reactance, flow unsteadiness
$M_{aO,l}$	Acoustic orifice linear reactance
$M_{aO,nl}$	Acoustic orifice nonlinear reactance
M_{aC_f}	Acoustic reactance, developing viscous flow
ζ	Damping coefficient
K_d	Nonlinear loss coefficient
Δc_p	Orifice pressure drop
x	Position vector
m	Mass
j	Square root of negative one
t	Conventional time
v	Velocity
ω	Angular frequency
P	Pressure
F	Force
L	Lift force
T	Temperature
Q	Volumetric flow rate
I	Current
Z	Impedance
R	Resistance
C	Capacitance
M	Inductance
c	Speed of sound
ρ	Fluid density
S	Stokes length
μ	Dynamic viscosity
ν	Poisson's ratio
γ	Specific heat ratio
V_∞	Free stream velocity
α	Angle of attack
C_L	Coefficient of lift
C_D	Coefficient of drag
C_M	Coefficient of pitching moment
C_f	Skin friction coefficient
E	Young's modulus
A_w	Hot wire probe surface area
R_w	Hot wire probe resistance
T_w	Temperature generated by hot wire probe
T_s	Surrounding flow temperature
h_T	Convective heat transfer coefficient
E_{HW}	Voltage measured by HW anemometer
E_{WT}	Voltage measured by WT strain gauge

ABBREVIATIONS

MEMS	Micro Electro-Mechanical Systems
AFC	Active Flow Control
ZNMF	Zero-Net-Mass-Flux
SJA	Synthetic Jet Actuator
K-H	Kelvin-Helmholtz
T-S	Tollmien-Schlichting
LEM	Lumped Element Modeling
CFD	Computational Fluid Dynamics
DNS	Direct Numerical Simulation
HWA	Hot Wire Anemometer
DAQ	Data Acquisition
TE	Trailing Edge
WT	Wind Tunnel
AoA	Angle of Attack
a	Acoustic
D	Diaphragm
C	Actuator Cavity
N	Neck or Nozzle
O	Orifice or Slot
aO,l	Acoustic-Orifice-Linear
aO,nl	Acoustic-Orifice-Nonlinear
<i>Model-C</i>	Single Diaphragm, Circular Orifice
<i>Model-R</i>	Single Diaphragm, Rectangular Slot
<i>Model-D</i>	Double Diaphragm, Circular Orifice

ABSTRACT

Priyanka Pagadala MSAE, Embry-Riddle Aeronautical University, June 2015. Design of Synthetic Jet Actuator for Flight Control of Small UAV.

The main idea of this project is to develop a prototype SJA - Synthetic Jet Actuator to embed into a small UAV with modified Glauert wing cross-section for Active Flow Control. Apart from lift enhancement, drag reduction, or separation control, etc; LCO suppression might be possible by modifying the boundary layer through the use of these actuators. For initial investigation, a wing section with span of 12.4 *cm* and chord of 14 *cm* was fabricated and tests were conducted in the subsonic wind tunnel at the free stream velocities of 5 and 10 *m/s*. From these experiments, lift curves for two different cases (with and without the actuator) were compared.

Two models of actuators, one with circular orifice and the other with rectangular slot, were developed using Gallas LEM tool. Effect of orifice shapes on the performance of the actuator is also investigated. Numerical analysis of 3D model was done in *Ansys Fluent* with $k-\epsilon$ turbulence model. Hot Wire Anemometer experiments were conducted to obtain frequency response plots to be validated with the similar plots obtained from the LEM tool. Due to the time consuming nature of CFD simulations, high accuracy reduced order models play a prominent role in quickly understanding the performance parameters that affect the jet. Further research is recommended for building or improving the current mathematical model and numerical tool to allow more sophisticated design configurations and optimization procedures.

1. Flow Control using Synthetic Jets

The idea of using Synthetic Jet Actuators has been the focus of flow control research for many years as they have the potential to influence the flow characteristics and aerodynamic performance of an airfoil. Before getting into the details of synthetic jet actuators, it is important to understand the purpose of flow control and which category these actuators fall into. Flow control involves active or passive devices which affect the desired or beneficial changes to the flow. Whether the task is to suppress or enhance the turbulence, prevent or provoke the separation, or to delay or advance the transition; useful end results include mixing augmentation, lift enhancement, flow-induced noise separation, reduction of drag, controlling moments, etc. All of this can lead to controlling more desired maneuvers if possible.

The ability to manipulate a flow field to get a desired change has gained more practical importance in the past century.

1.1 Evolution of Flow Control

Initial contributions to the science of flow control were done by introducing the boundary layer theory in 1904 by Prandtl, which laid the foundation of the scientific era. This explained the physics behind the separation phenomenon and also described several experiments in which a boundary layer was controlled.

Flow control has played a major role during the second world war, which led to the development of faster, more powerful, and highly maneuverable efficient aircraft, missiles, submarines, and ships, etc.

Later many industrialized countries invested in a search for methods of conserving energy. Drag reduction was given special importance during this period. Due to the availability of fast and inexpensive computers, the ability of recreating complex flow fields numerically opened new possibilities in areas where research had been difficult to approach analytically.

Most of the research on control devices was concentrated toward manipulating the coherent structures in transition and turbulent regimes. During this ongoing modern era, the ability to achieve large scale changes in the behavior of the flow with low level energy inputs is explored with theoretical advancements in deterministic chaos using MEMS - Micro Electro-Mechanical Systems and neural networks. With advancements in high performance computing power, more detailed DNS models are being researched (Gad-El-Hak, 2000).

1.1.1 Passive Flow Control

Passive flow control is related to the static structural modifications on the wing surface that can dictate the flow over it. These techniques include geometric shaping to manipulate the pressure gradient (Gad-El-Hak, 2000), e.g., fixed vortex generators for separation control or riblets on the surface to reduce drag.

1.1.2 Active Flow Control

Active control methods, in which energy inputs are introduced into the flow, have been emphasized in the past decade. Active control schemes can be divided into predetermined or reactive methods (Kral, 2000). Predetermined control methods involve giving steady and unsteady inputs that include jet vectoring using piezoelectric actuators (Smith & Glezer, 1997) and oscillatory blowing (Seifert & Pack, 1999). On the other hand, in reactive control methods, the power input to the actuator is continuously adjusted based on some sort of measurement element, such as a sensor. The control loop for reactive control can be either feed-forward, which is an open loop, or feed-back, which is a closed loop.

1.1.3 Reactive Control Loops

The sensor is placed upstream of the actuator in the feed-forward control loop. As flow structures pass through stationary sensors and actuators, the measured and the controlled flow field parameter will differ. The control must interact with turbulent fluctuations which are already present in the flow field. Manipulating these small scale turbulent fluctuations is a challenging problem.

With the feed-back control loop, to measure the flow parameters, a sensor is placed downstream of the actuator. The controlled variable is compared with the upstream reference variable. A feedback control law is utilized to control the energy introduced at the actuator (Moin & Bewley, 1994). Interactive feedback controls are classified

into four schemes based on the extent to which they are based on the governing flow equations: adaptive control, physical model-based, dynamical systems, and optimal control. Different types of active control strategies are shown in the below flow chart.

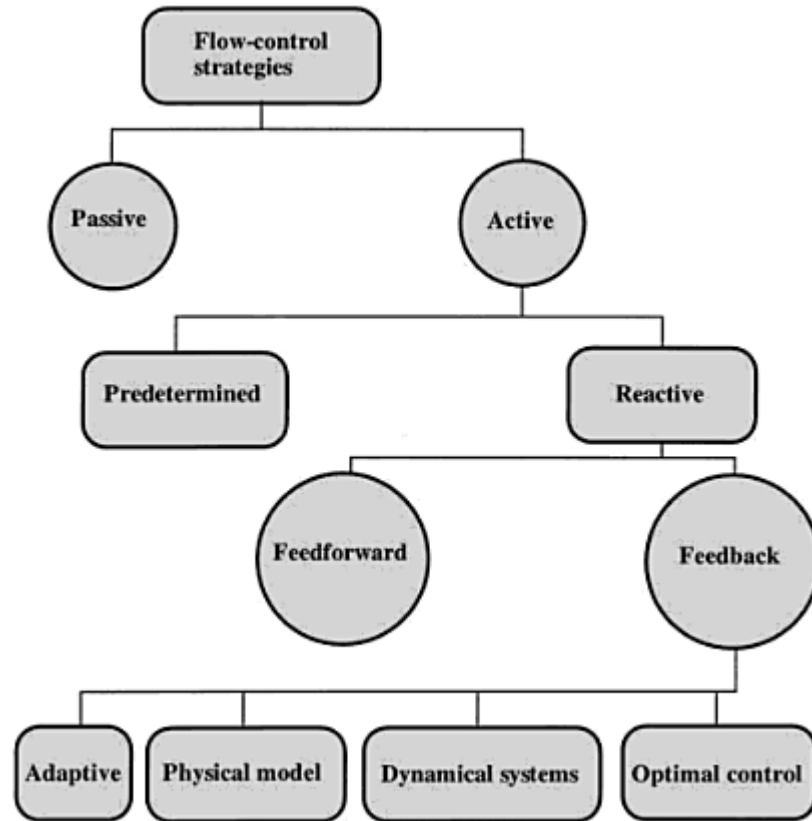


Figure 1.1.. Flow control strategies (Gad-El-Hak, 2000)

The future of feedback flow control as discussed by (Bewley, 1999) stated that research must be conducted at the intersection of the traditional fields of fluid mechanics, mathematics, and control theory for successful application of feedback control schemes.

1.1.4 Applied AFC Device

In aerospace applications, even though passive flow controls have useful features in improving aerodynamic performance, they can substantially increase the weight of the body, but not necessarily in every case. Thus it is important to choose passive control devices that will have good trade-offs between weight and performance, which is just as well true for active flow control devices.

Every control device has its own set of parameters to work with and unique features that need to be researched. Combination of some of these methods could also be possible, especially with a device like a synthetic jet actuator. Synthetic jets might be a combination of acoustic streaming and oscillatory blowing and suction. The devices that produce these type of jets for this research are known as Synthetic Jet Actuators or ZNMF - Zero-Net-Mass-Flux actuators, requiring no external fluid source. These devices are also suitable for feedback control and the peak velocities are limited to low to moderate subsonic speeds (Cattafesta & Sheplak, 2011). The following chapters give more detailed information on the synthetic jet advantages and challenges in the flow control application.

1.2 Synthetic Jet Actuators

Synthetic jets in flow control are characterized by their ability to perturb the flow from the orifice/slot. Proper characterization and understanding of the device and actuator operation is crucial for successful implementation.

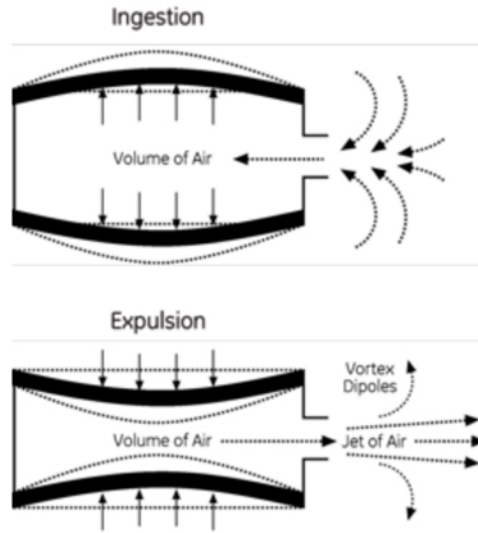


Figure 1.2.. Inflow and outflow vortex generation (Mohseni & Mittal, 2014)

The developing vorticity from the jet imparts non-zero momentum even though these devices are considered as ZNMF. By adjusting pressure using piezoelectric diaphragm vibration, pulsed jets release energy from the opening to manipulate the boundary layer on the body. These pulsing jets might induce energy near to the surface, thus affecting the local as well as the global characteristics of the flow.

When exposed to a moving boundary produced from the SJA, some unstable frequencies might be triggered on the free stream boundary layer and significantly affect the dynamics of the flow. Changes in velocity profiles and pressure gradients could lead to amplifying instabilities such as Kelvin-Helmholtz, Rayleigh-Taylor, or streamwise T-S instabilities.

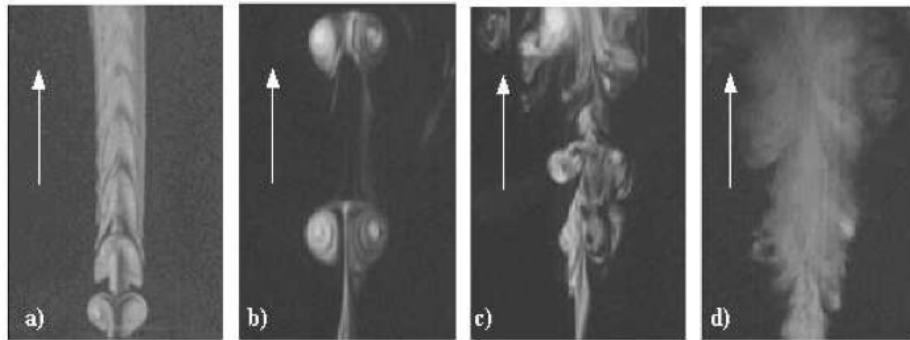


Figure 1.3.. Formation of synthetic jets based on the Reynolds number (Holman, 2006)

With internal flow from the cavity on one side and the ambient external flow on the other side, an inherent asymmetry develops, and so it is important to study the development of the flow over multiple cycles (Glezer & Amitay, 2002).

As discrete vortex pairs ultimately undergo transition to turbulence, the evolution of the synthetic jet flow can be divided into two distinct domains:

1. Near the jet exit plane, flow is dominated by the time periodic vortex formation.
2. Fully developed turbulent flow.

These two distinct domains are very important to keep in mind when the SJA is interacting with the external flow. Vortex formation near the jet exit plane depends on every design parameter. Each vortex pair from the jet develops a spanwise instability and ultimately undergoes transition to turbulence, slows down, or loses its coherence and becomes indistinguishable from the mean flow. Therefore, it is vital to idealize the synthetic jet actuator from the mean flow and study it independently for better performance of the actuator (Smith & Glezer, 1997).

Spatial time average exit velocities \overline{V}_j are very important flow parameters to take into account and these can be used to characterize the jet flows from the orifice (Glezer & Amitay, 2002).

The main advantage of these devices over other Active Flow Control devices is that these work on the surrounding fluid and do not require any extra fluid storage or source.

Decades of research had been carried out in understanding the jet criteria, interactions with the mean flow, numerical studies, and design implementation. A brief summary of this history is given in the literature review.

1.2.1 Literature Review

Much research had been done to characterize and study the behavior of synthetic jet actuators experimentally and numerically. (James, Jacobs, & Glezer, 1996) investigated the behavior of the jet by submerging the oscillating diaphragm model in water. Experimental investigation by (Smith & Glezer, 1997) showed that synthetic

jets are dominated by the time periodic formation of the vortical structures near the exit plane of the jet. They investigated the dynamics of the actuator. (Golmes, Crowther, & Wood, 2006) experimentally investigated the effect of geometry and the actuation variables on the peak jet velocities of the actuator.

Low fidelity analysis tool was first developed by (Rathnasingham & Breuer, 1997). Their tool can predict the magnitude of the jet peak velocity V_j for a given input of power. (Carpenter & Lockerby, 2004) developed an SC - Static Compressible model that can predict the optimal cavity and orifice heights $\{h_C, h_N\}$. (Gallas, 2002) developed a lumped element model into a low fidelity analysis tool where different energy domains were coupled and the equivalent electric circuit was represented to get the frequency response profile. Most of his work was concerned with the design optimization of synthetic jet actuators. (Holman, 2006) worked on the the experimental investigation of flow through ZNMF actuators. Cavity effects on the jet exit velocity of the piezoelectric actuator was investigated by (Mane, Mossi, Rostami, Bryant, & Castro, 2007). Later, by incorporating different equations for orifice shapes (circular and rectangular) for the actuator, the LEM technique has been refined by (Gallas, Holman, & Cattafesta, 2005).

(Ugrina & Flatau, 2004) investigated the jet actuator design parameters by studying different shapes and types of diaphragms, as well as investigating nozzle and orifice shapes. Evolution of the jet and the jet criterion of synthetic jets was investigated by (Glezer & Amitay, 2002), giving insight on the global effects of the flow in the near field and the far-field region. Acoustic streaming for flow control applications

and Micro propulsion using Navier-Stokes simulations and a preliminary study on SJA towards a complete control of MAV was done by (Golubev & Mankbadi, 2009) and (Golubev, Mankbadi, & Nakhla, 2009). Instead of moving control surfaces, synthetic jets were mounted on the leading and trailing edges of the modified NACA 65₂ – 215 swept wing section, taking note of the drag and lift coefficients and showing substantial lift increments using lift curve plots (Sefcovic & Smith, 2010).

1.2.2 Current Research

In this thesis, single diaphragm actuators *Model-C* (prototype with circular orifice) and *Model-R* (prototype with rectangular slot) were designed and developed using the Gallas LEM analysis tool and their frequency responses are validated against Hot Wire Anemometer experiment results. Shape effects of these two models were investigated using 3D models in *Ansys Fluent*. Later, a modified Glauert small scale wing section was developed and the actuator was placed inside it. Lift curve plots of the clean case without the actuator as well as cases with the SJA embedded were compared to each other.

2. Lumped Element Modeling

Low fidelity analysis tools are important for the process of selecting the actuator's parameters. In order to gain an overview of large parametric space without time consuming simulations or developing prototypes, parameters need to be studied. Lumped Element Modeling uses circuit analogy to couple between electrical, mechanical, and acoustic domains. In an electroacoustic system, differential pressure and voltage are *effort variables*, while current and volumetric flow rate are *flow variables*.

When electrical input E_δ is given to the diaphragm of the actuator, it starts to displace the air from the cavity ΔV_δ . The diaphragm system is similar to a coupled spring-mass-damping system. There are mainly two Fundamental frequencies for the synthetic jet actuators:

1. Diaphragm fundamental mechanical frequency ω_D
2. Helmholtz acoustic resonance frequency ω_H

2.1 Gallas LEM

Currently, the model used is the Gallas LEM model for synthetic jet actuators, which operates under certain assumptions.

2.1.1 Assumptions

(Gallas, Holman, & Cattafesta, 2005) makes the assumption in their LEM model that the wavelength λ_δ of the pressure oscillation will be much greater than the dimension of the device, as visualized in figure 2.1.

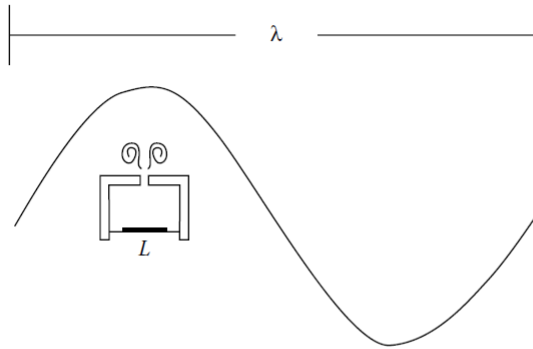


Figure 2.1.. LEM λ_δ assumption (Mohseni & Mittal, 2014)

If this assumption holds, the spatial and the temporal domains are independent of each other and the center-line exit velocity of the jet V_j can be obtained as output impedance in the circuit analogy. Section 2.1.2 below explains this LEM model in detail. This model is also hypothesized assuming fully developed Poiseuille or pipe flow (Gallas, Holman, & Cattafesta, 2005).

2.1.2 Circuit Details

The acoustic domain is also modeled in electrical domain with variables associated by D -diaphragm, C -cavity, N -neck, and O -orifice as subscripts for components.

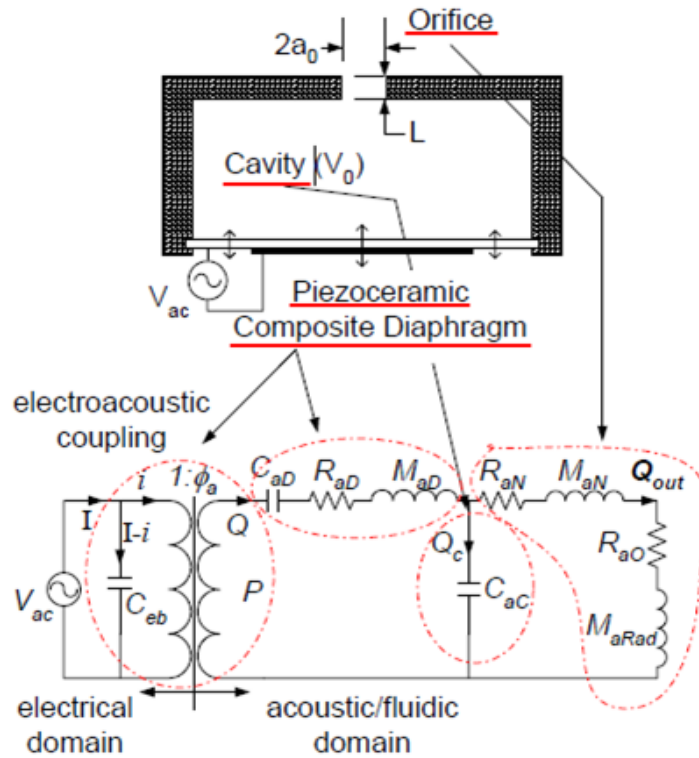


Figure 2.2.. Circuit representation components (Gallas, Sheplak, & Cattafesta, 2005)

The circuit in figure 2.2 is reduced down to the below circuit in figure 2.3 with impedances. The derivation can be found in the (Gallas, Holman, & Cattafesta, 2005) paper on dynamics of isolated Zero-Net Mass-Flux actuators.

With the same units as resistance, Impedance is represented as a complex quantity where the real part is the resistance and the imaginary part is the reactance, which is

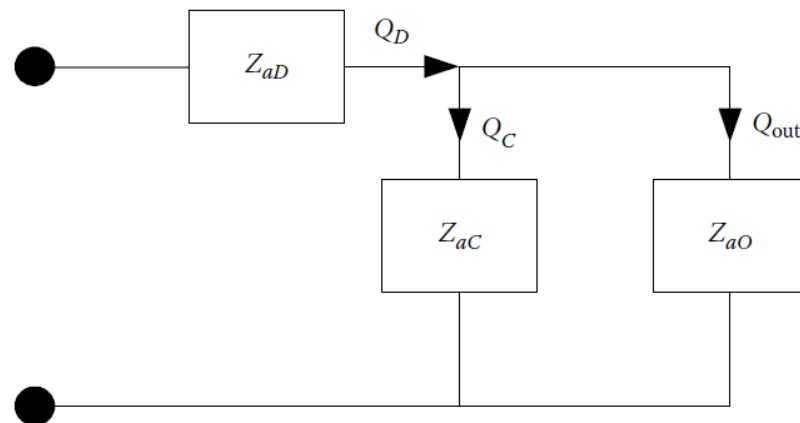


Figure 2.3.. Circuit representation impedances (Mohseni & Mittal, 2014)

obtained from capacitance and inductance. As shown in the figure, each component is related to a certain impedance.

2.1.3 Refined LEM

The refined LEM has additional parameters that are taken into consideration, mainly concerned with improving the component of the acoustic impedance of the orifice Z_{aO} . In figure 2.4 the flow chart of the LEM technique explains the method to compute the frequency response and the jet exit velocity V_j of the isolated synthetic jet actuator.

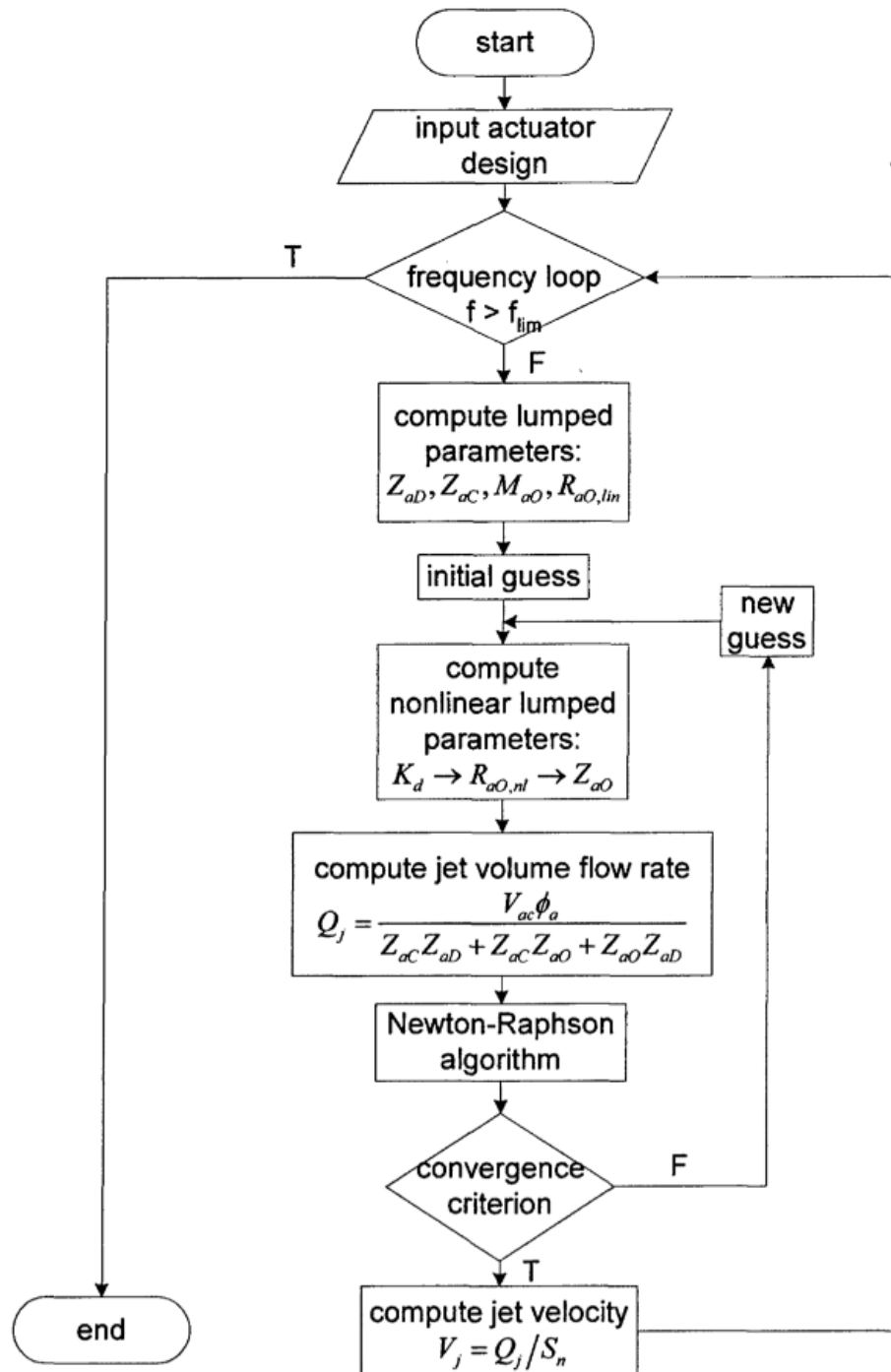


Figure 2.4.. Refined LEM technique to obtain $\{\omega_\delta, V_j\}$ frequency response plot for jet exit velocities (Gallas, Holman, & Cattafesta, 2005)

2.1.4 Orifice Physics

The detailed control volume analysis of the orifice flow physics was provided in (Gallas, Holman, & Cattafesta, 2005) and the final output is shown here in figure 2.5:

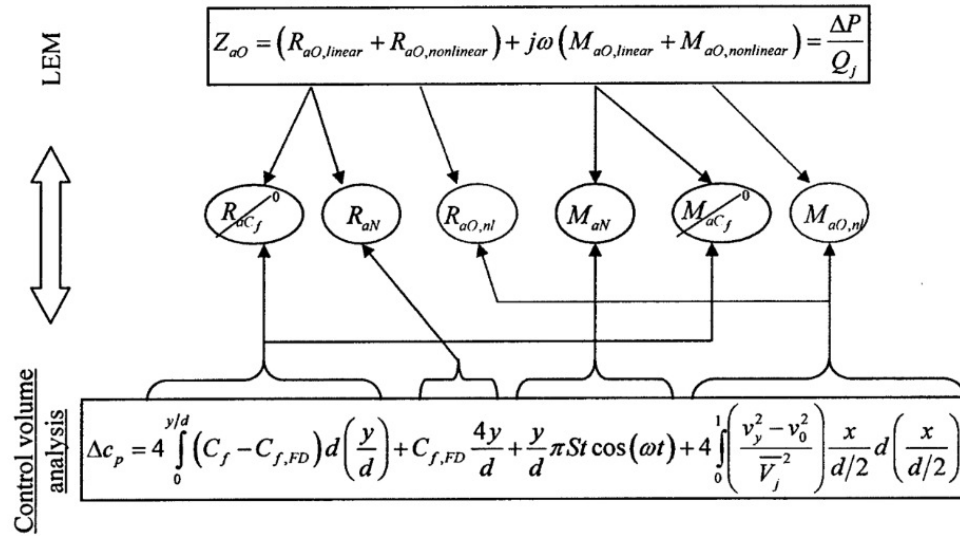


Figure 2.5.. Comparison between control volume terms and the impedance of orifice (Gallas, Holman, & Cattafesta, 2005)

Acoustic impedance of the orifice Z_{aO} is a combination linear and nonlinear resistances and reactances relating to the pressure variation ΔP and the output volumetric flow rate Q_j .

$$Z_{aO} = (R_{aO,nl} + R_{aO,l}) + j\omega_\delta(M_{aO,l} + M_{aO,nl}) = \frac{\Delta P}{Q_j} \quad (2.1)$$

The analytical terms from the control volume analysis represent the linear resistance term, $R_{aO,l} = R_{aC_f} + R_{aN}$, as a combination of linear resistance due to starting

developing viscous flow R_{aC_f} and the resistance due to fully developed viscous flow R_{aN} . However, R_{aC_f} is neglected in the Gallas LEM and the resultant simplifies to:

$$R_{aO,l} = R_{aN} \quad (2.2)$$

Linear reactance, $M_{aO,l} = M_{aC_f} + M_{aN}$, is a combination of reactance due to starting developing viscous flow M_{aC_f} , which is neglected, and the reactance due to unsteadiness of the flow M_{aN} . The nonlinear reactance $M_{aO,nl}$ is due to the velocity momentum.

Nonlinear acoustic resistance for the orifice $R_{aO,nl}$ represents the nonlinear losses taking orifice shapes through K_d into account, and is given by

$$R_{aO,nl} = \frac{\rho K_d Q_j}{2S^2} \quad (2.3)$$

This term, $R_{aO,nl}$, is a function of the volume flow rate Q_j and corresponds to the nonlinear entrance and exit region effects. These are approximated by modeling the nonlinear resistance of the orifice as a generalized flow meter. (McCormick, 2000). At higher frequencies, the velocity profile in the orifice is modeled as a circular duct driven by the oscillating pressure diaphragm, where the velocity is proportional to the pressure gradient (Mohseni & Mittal, 2014).

$$\Delta c_p = \frac{2\Delta P_C}{\rho \overline{V_j^2}} \quad (2.4)$$

The equation between the orifice loss coefficient K_d and nonlinear part on Δc_p makes everything interrelated:

$$K_d = \Delta c_{p,nl} \frac{4}{\pi^2} \quad (2.5)$$

K_d is the steady pipe flow nonlinear dump loss coefficient for the orifice nozzle.

$$Z_{aO,nl} = R_{aO,nl} + j\omega_\delta M_{aO,nl} \quad (2.6)$$

$Z_{aO,nl}$ cannot be solved for both resistance and reactance. The phase lag from the nonlinear term or the reactance due to velocity momentum is neglected. (Gallas, Holman, & Cattafesta, 2005).

Finally, it is noted that LEM accounts for

- Viscous effects for fully developed flows R_{aN} ,
- Flow unsteadiness M_{aN} , and
- Nonlinear resistance due to velocity momentum $R_{aO,nl}$.

It discards or neglects

- Viscous effects of starting developing flow R_{aCf}
- Phase lag from the nonlinearities $M_{aO,nl}$.

In the below table, the computation differences between shapes for modeling the orifices are shown, mainly circular and rectangular.

Table 2.1.. Difference in shapes for orifice (equations)

		Circular	Rectangular
Q_D	(m^3/s)	$j\omega_D\Delta\forall_\delta$	$j\omega_D\Delta\forall_\delta$
ω_H	(s^{-1})	$\sqrt{\frac{3\pi(d_O/2)^2c^2}{4h_N\forall_\delta}}$	$\sqrt{\frac{5w_O(d_O/2)c^2}{3h_N\forall_\delta}}$
R_{aN}	(kg/m^4s)	$\frac{8h_N\mu}{\pi(d_O/2)^4}$	$\frac{3h_N\mu}{2w_O(d_O/2)^3}$
M_{aN}	(kg/m^4s)	$\frac{4h_N\rho}{3\pi(d_O/2)^2}$	$\frac{3h_N\rho}{5w_O(d_O/2)}$
ζ		$12\frac{\omega_\delta}{\omega_H S^2}$	$5\frac{\omega_\delta}{\omega_H S^2}$

These two have different impedance terms as well as damping coefficients due to alternate resistance and reactance terms which can incorporate the properties of these shapes. Initial design parameters were selected using the same open surface area A_O among the circular orifice and rectangular slot. Based on LEM plots, the experimental models were developed.

2.1.5 Results

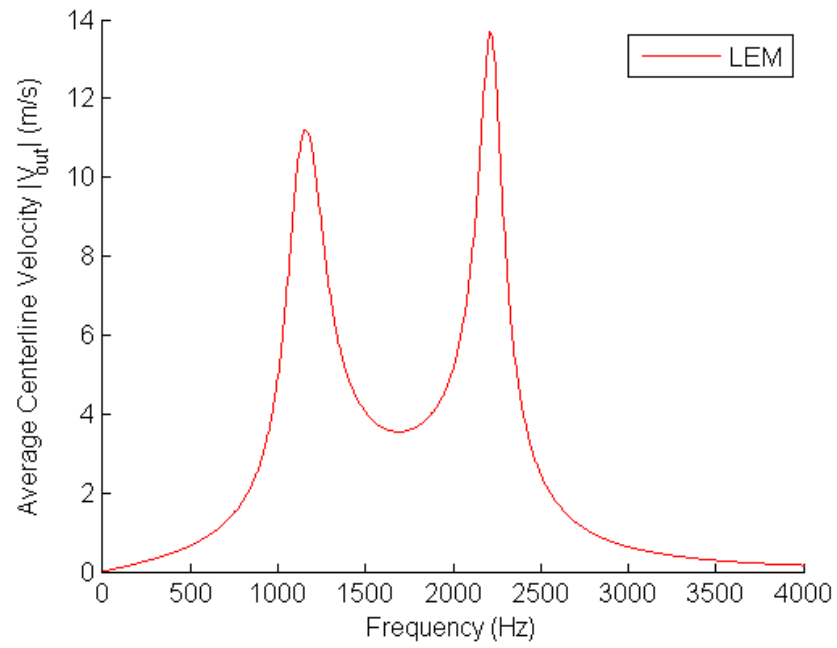


Figure 2.6.. LEM result for *Model-C* $\{\omega_\delta, V_j\}$

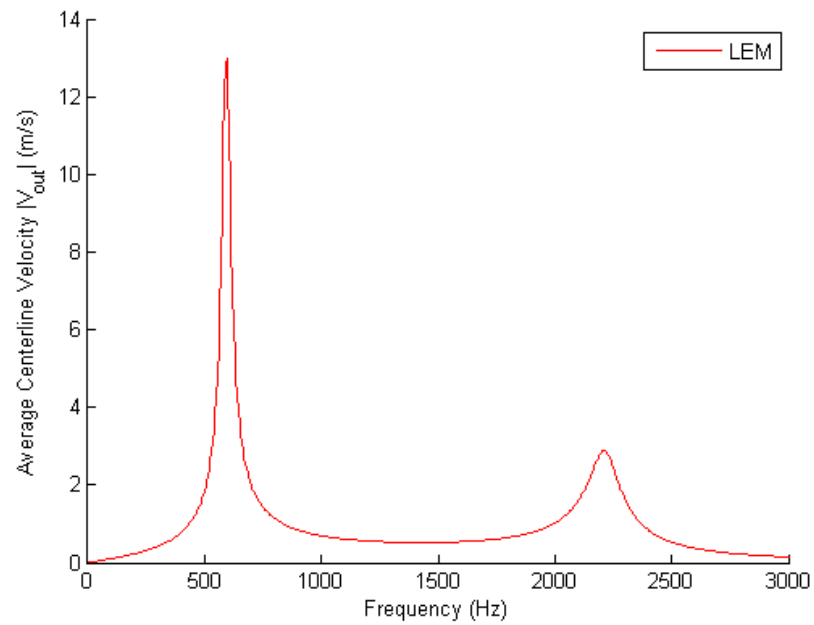


Figure 2.7.. LEM result for *Model-R* $\{\omega_\delta, V_j\}$

2.2 Development of an Actuator

The initial design parameters for the cavity were selected based on the small scale wing configuration so that the actuator can be embedded. Orifice dimensions are selected for the effective measurements from the HWA experiments. The diameter of the actuator orifice d_O is almost equal to the the hot wire probe length, helping towards predicting the velocities with more accuracy. Many design parameters were investigated before selecting the initial design configuration, these include different cavity heights, widths, and lengths $\{h_C, w_C, l_C\}$; as well as different diaphragm parameters such as shim-to-piezo diameters and shim and piezo thicknesses $\{d_D, t_D\}$; and different orifice shapes with same areas A_O to obtain maximum V_j peak velocity.

2.2.1 Actuator Geometry

Similar geometry is used for the SJA with circular and rectangular slot. The geometrical parameters are provided in the tables:

Table 2.2.. Geometric parameters for acuators *Model-C* and *Model-R*

			Circular	Rectangular
			<i>Model-C</i>	<i>Model-R</i>
Orifice/Slot Diameter	d_O	(mm)	2.5	1.6
Slot Width	w_O	(mm)	-	3
Orifice/Slot Length	h_N	(mm)	0.5	0.5
Cavity Height	h_C	(mm)	50	50
Cavity Length	l_C	(mm)	40	40
Cavity Width	w_C	(mm)	3	3
Voltage Applied	E_δ	(V)	25	25

2.2.2 Diaphragm Boundary

Table 2.3.. Selected piezoelectric diaphragm properties

			Piezoceramic	Shim
Young's Modulus	E	(pa)	6.3×10^{10}	8.9×10^{10}
Poisson's Ratio	ν		0.4	0.331
Density	ρ	(kg/m^3)	8600	7500
Thickness	t_D	(mm)	0.3	0.23
Diameter	d_D	(mm)	23	35

The diaphragm boundary condition is a very important aspect and has a significant impact on the performance and also on the design of an actuator. LEM assumes a clamped boundary condition, which creates a fixed boundary.

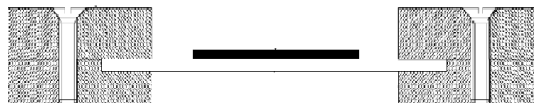


Figure 2.8.. Clamped boundary (Mohseni & Mittal, 2014)

At the clamped boundary near the edges, transverse radial displacement is zero, while there is a finite radial displacement for the rest of the diaphragm. This can be achieved by sandwiching metal plates with a sealed portion having the approximate thickness of the shim.

Another type of boundary can be created by using o-rings, which is a pinned boundary. In practice, it is hard to achieve this type of boundary condition. When two o-rings on either side of the diaphragm are used, they cease the diaphragm from displacement and instead allow rotation with zero radial displacement.



Figure 2.9.. Pinned boundary (Mohseni & Mittal, 2014)

There are other practices like rubber gasket. The boundary condition for these types is somewhere between the pinned and clamped condition. A clamped boundary is used in the development of an actuator.

2.2.3 Prototype

Four plates were screwed together with a cavity compartment between them. Two plates are used to mount the diaphragm as a clamped boundary as discussed on page 22. The diaphragm used is the Murata 7BB-35-3LO, having a shim diameter of 35

mm and a piezoceramic d_D of 23 mm . As already discussed two different orifice shapes were developed, *Model-C* has the circular orifice and *Model-R* is changed to a rectangular slot. Since individual plates were used in the development of models, this gives flexibility to try the actuator with double diaphragms and circular orifice using *Model-D*. Later HWA experiments were conducted at various frequencies to obtain a frequency response graph with the current models and to validate with the results from the plots of the LEM results. Different models are shown in the figures below.

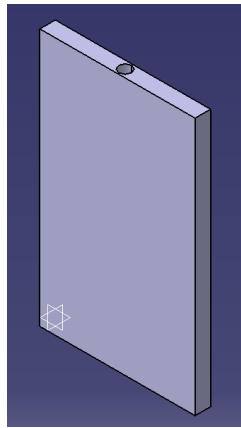


Figure 2.10.. Circular orifice geometry in CATIA from *Model-C*

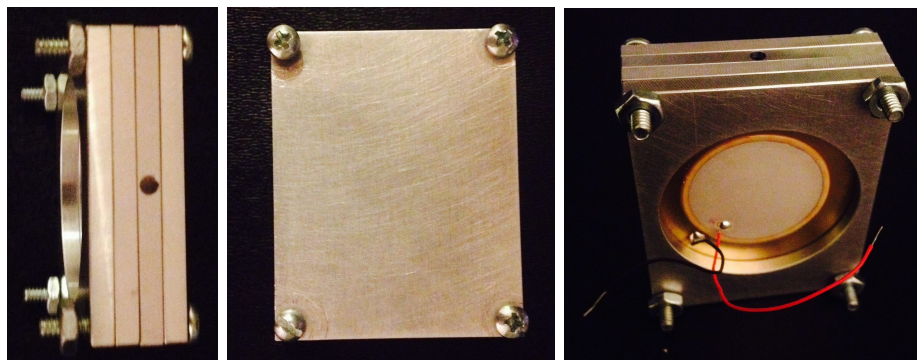


Figure 2.11.. Circular orifice actuator, prototype *Model-C*

3. Computational Fluid Dynamics

3.1 CAD Geometry and Meshing

As already mentioned, the geometry has been selected using an LEM low fidelity analysis tool. Equal areas A_O are used in order to compare and understand what the differences in shape effects can be when the circular orifice and the rectangular slot are compared. Separate 3D models of the actuator geometries were made in *CATIA*. Figure 3.1 below shows the rectangular slot model of geometry. For 2D numerical simulations, both geometric shapes for the orifice have similar dimensions and can be ambiguous. Therefore, 3 dimensional models are used to obtain the velocity profiles from the differing geometries.

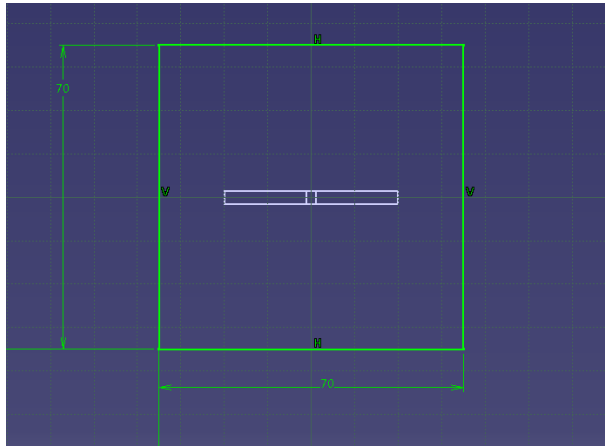


Figure 3.1.. SJA and ambient domain geometry top view for *Model-R*

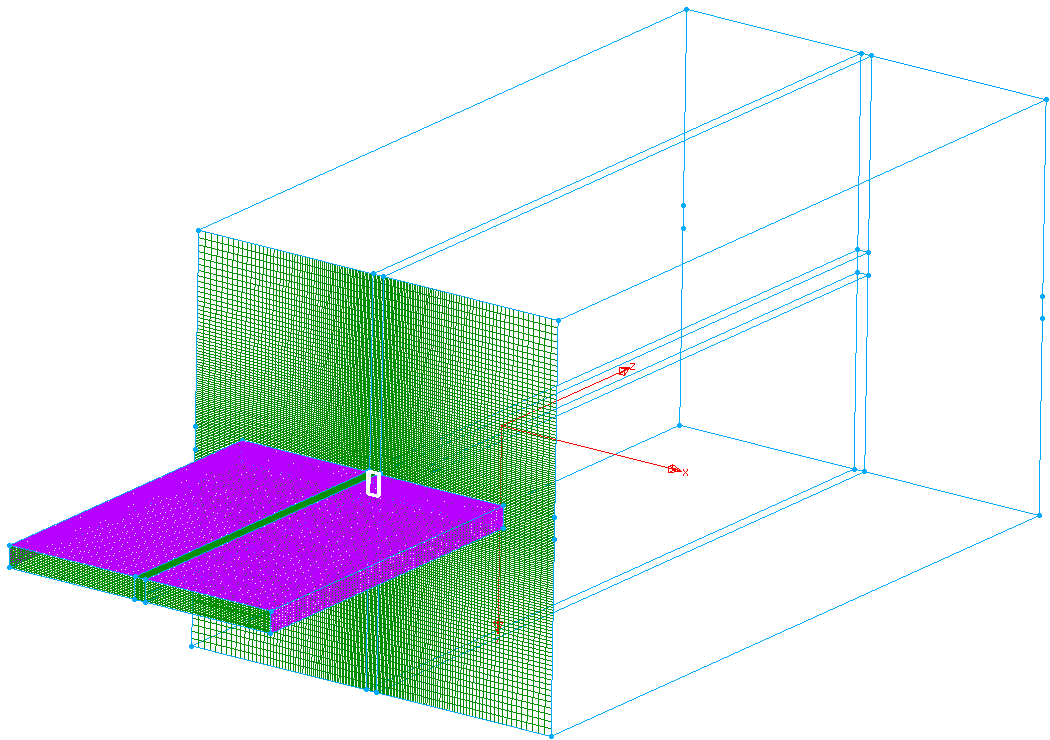


Figure 3.2.. Meshed SJA with ambient air computational domain

In order to translate the geometry into the solver it must be converted into a meshed computational domain. To accomplish this, *Pointwise* was used to make structured meshes.

3.1.1 Rectangular Slot

As *Model-R* involves no round edges, it is easy to discretize into an unskewed structured hexahedral grid. Several additional guidelines, domains, and blocks are

created and boundaries are set. The piston is a velocity inlet, the rest of the cavity and orifice are walled. Orthogonal to the orifice is a wall representing the wing's surface. The top ambient surface is a pressure outlet and the ambient sides are pressure inlets.

3.1.2 Circular Orifice

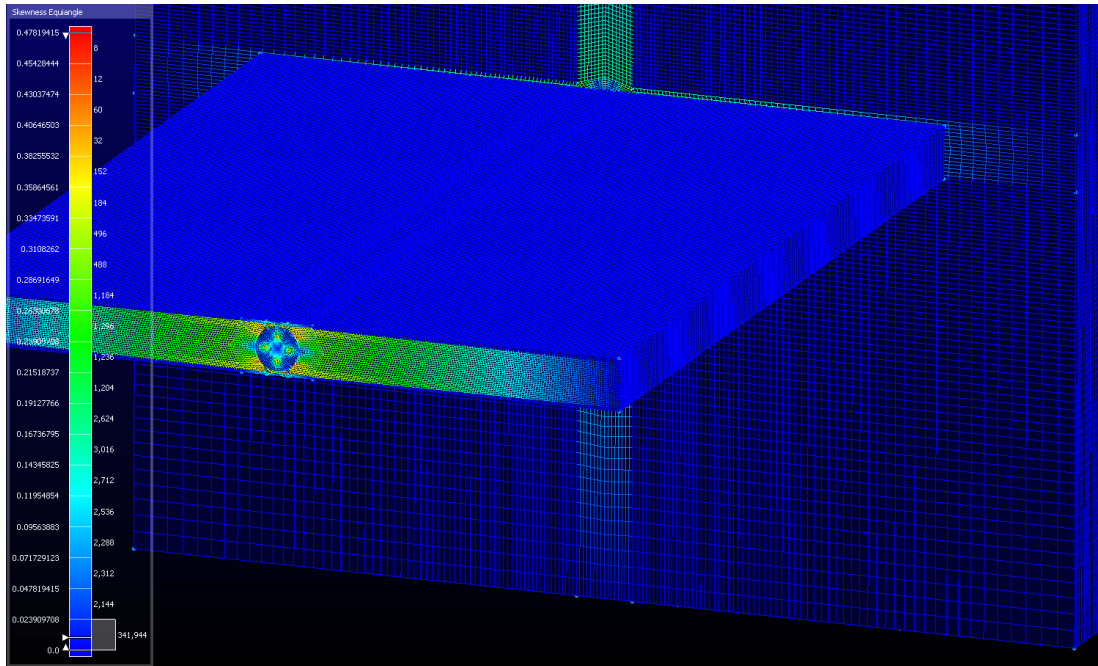


Figure 3.3.. Equiangle skewness in *Model-C* computational mesh

In order to achieve structured hexahedral mesh for the areas surrounding the circular orifice, some additional construction edges needed to be created in order to limit maximum skewness to approximately 0.4. The boundaries are set similarly to the mesh settings for the rectangular slot.

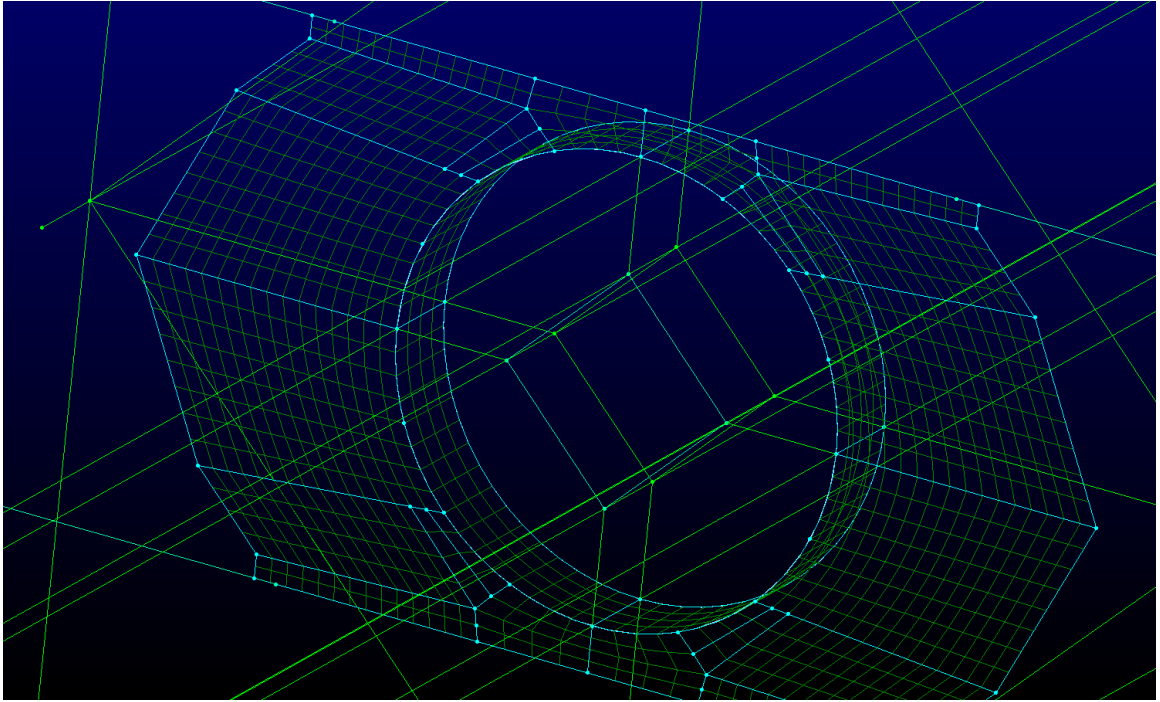


Figure 3.4.. Construction lines for circular orifice

3.1.3 Mesh Independence

For grid independence studies, coarse 3/4, medium 1/1, and fine 5/4 meshes are used to verify that the results converge similarly after multiple cycles of operation. Cell counts for the meshes include 7524244 for the actuator *Model-C* and 5240572 with the rectangular *Model-R*. When doing mesh independence, the sizes for the rectangular domains would become 2190112 and 10312400 cells for the comparisons.

For comparison, all three mesh sizes were used to capture a velocity profile after five cycles at $t = 3.009 \times 10^{-3}$ with 928 time steps and plotted together. All three of the results show very similar results and practically equal V_j exit velocities in figure

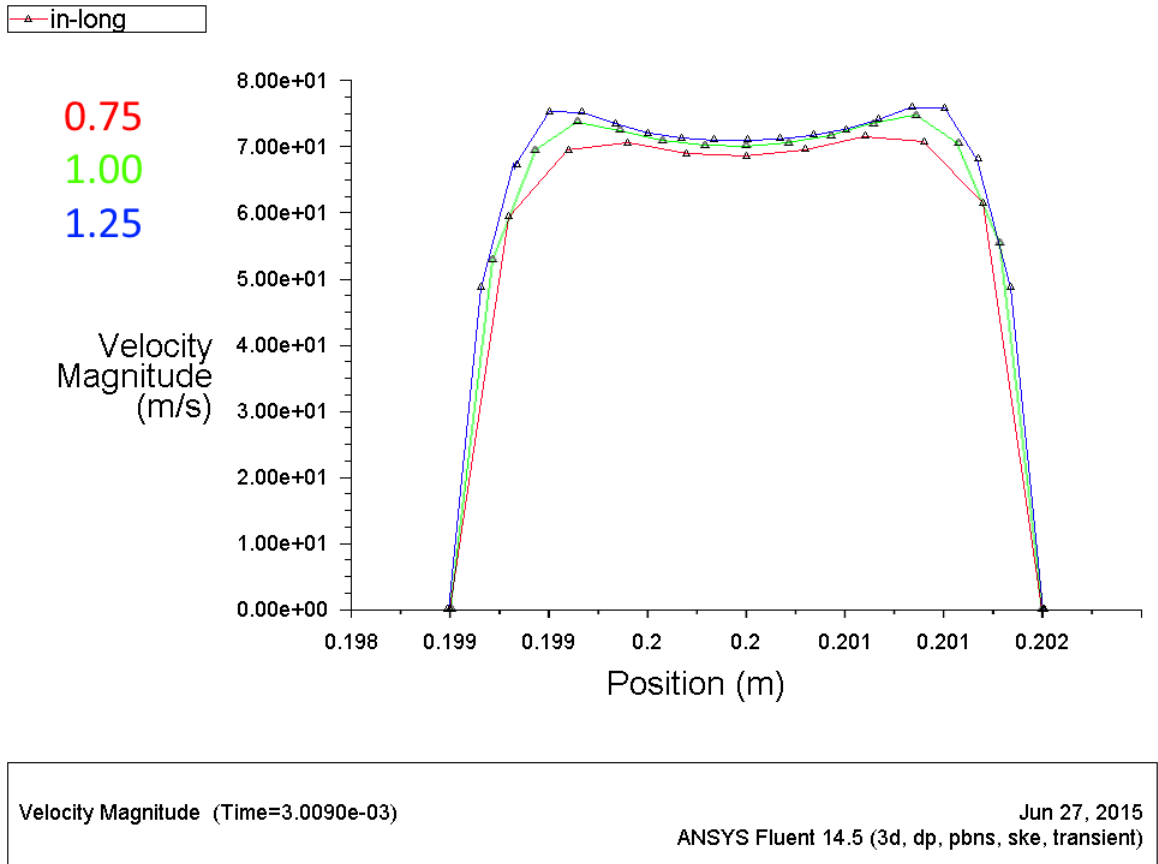


Figure 3.5.. Velocity profile mesh independence comparison $\{d_o, V_j\}$

3.5. The finer mesh of course displays more fine details that can be made out in the shape of the velocity profiles.

3.2 Numerical Solution

Commercial *Fluent* 14.5 solver is used for the solution. The following sections detail some of the solver specifications.

Nearly all the flows in nature are transient. The steady state assumption only holds if transient fluctuations have been ignored. Naturally occurring transient flow is due to the growth of instabilities or non-equilibrium states of the fluids, while with forced transients, the source drives the flow field.

Forced transients mostly have time dependent boundary conditions and a time periodic solution where flow variables fluctuate with repeating patterns. In *Fluent*, boundaries for these types of flows use a UDF (User Defined Function) that is dependent on time. The UDF δ for modeling E_δ at this boundary is discussed in more detail in section 3.2.2.

In order to accurately resolve the flow field of the governing Navier-Stokes equations, turbulence modeling is needed.

3.2.1 Turbulence Model

The k - ϵ turbulence model is the most popular and widely used for the simulations. This is also the most common model used in CFD that simulates the characteristics of the mean flow for turbulent flow conditions. (Mane et al., 2007).

- Energy in the turbulence can be determined from the first transport variable k which is Turbulent Kinetic Energy.
- Turbulent Dissipation Rate ϵ is the second transport variable that determines the dissipation rate.

The two governing transport equations are the PDEs which give the general description of the turbulence. For the standard k - ϵ model, the turbulent kinetic energy is solved using equation 3.1 and the dissipation rate with 3.2.

$$\frac{\partial(\rho k)}{\partial t} + \frac{\partial(\rho k u_i)}{\partial x_i} = \frac{\partial}{\partial x_j} \left[\frac{\mu_t}{\sigma_k} \frac{\partial k}{\partial x_j} \right] + 2\mu_t E_{ij} E_{ij} - \rho \epsilon \quad (3.1)$$

$$\frac{\partial(\rho \epsilon)}{\partial t} + \frac{\partial(\rho \epsilon u_i)}{\partial x_i} = \frac{\partial}{\partial x_j} \left[\frac{\mu_t}{\sigma_\epsilon} \frac{\partial \epsilon}{\partial x_j} \right] + C_{1\epsilon} \frac{\epsilon}{k} 2\mu_t E_{ij} E_{ij} - C_{2\epsilon} \rho \frac{\epsilon^2}{k} \quad (3.2)$$

Which means the rate change and the transport of the turbulent kinetic energy or dissipation rate is equal to the transport by diffusion and rate of production and destruction of the kinetic energy or dissipation rate.

Pressure-Implicit with Splitting of Operation (PISO) options were used for the circular orifice to have more accurate simulations of pressures and velocities in the hexahedral control volumes due to skewness in the mesh. PISO is based on a high degree of approximation between the iterative corrections, which significantly reduces the difficulties with the convergence.

3.2.2 Boundary Conditions

Boundary conditions provide the information about the way fluids interact with their surroundings. Numerically, fixing boundary conditions to the model provides external velocity information to the differential equations.

Wall Boundary Condition

Normally wall conditions use a no-slip boundary condition. This condition states that there is no relative motion between the particles of the fluid v_f and wall surfaces v_w or solid boundaries.

$$v_f = v_w \quad (3.3)$$

When $v_w = v_f = 0$ the wall is stationary and if this value changes, the flow at the boundary is altered.

Diaphragm Boundary Condition

Due to the oscillating diaphragm deflection δ , the boundary condition deals with changes in velocity. To model the effect of this behavior, a user defined function is created with the $\delta(t) = \delta_x \sin(\omega_\delta t)$ waveform, corresponding to the input signal E_δ but neglecting the piezoelectric coupling of the mechanical and electrical domains. Actual displacements at the boundary of the mesh is not taken into account (Bourlier, 2010).

$$v_\delta(t) = \frac{\partial \delta}{\partial t} = \omega_\delta \delta_x \cos(\omega_\delta t) \quad (3.4)$$

This function $v_f = v_\delta(t)$ is given as a time dependent velocity boundary condition on the cavity-piston domain. As this models the diaphragm as a flat rectangular

piston, more precise calculations with additional degrees of freedom and a circularly clamped diaphragm require the adaptive time step and a spatially moving boundary.

$$\delta_x = \frac{v_\delta}{\omega_\delta} = \frac{A_O V_j}{A_D \omega_\delta} \quad (3.5)$$

The deflection δ_x of the diaphragm was estimated by taking the incompressible limit into account and is calculated by taking the area of the piston A_D and the orifice neck A_O into consideration with the Bernoulli principle.

Using a programmed user defined function, this behavior is translated into the *Fluent* solver according to SI units. The final amplification of the end results depends on what approximate V_j is desired under incompressible limit assumption.

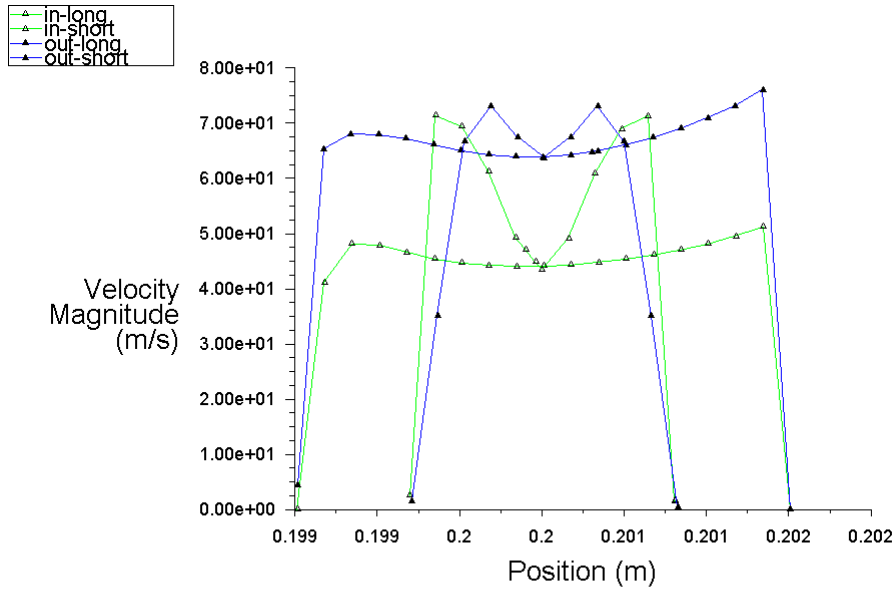
3.2.3 Time Stepping

To calculate the time step size Δt , the inverse of the sampling frequency f_s is used. This number is obtained by computing the number of time steps $n \in \mathbb{N}$ desired per period T_δ of waveform oscillation.

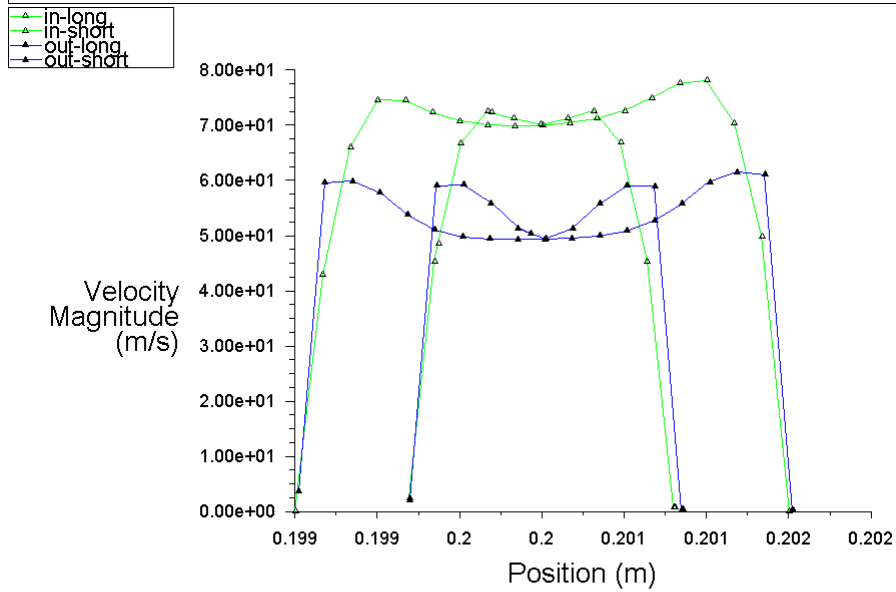
$$\Delta t \approx f_s^{-1} = \frac{T_\delta}{n} = \frac{2\pi}{\omega_\delta n} \quad (3.6)$$

For these numerical experiments $n \approx 185$ is used with operating frequencies of 1800 *Hz*. Thus, using some rounding, for $\omega_\delta = 2\pi \times 1800 \rightarrow \Delta t = 3 \times 10^{-6}$ *s*. Simulations were carried out for different cases. For numerical simulations in *Ansys Fluent* the maximum number of iterations per time step is set to 9.

3.3 Results

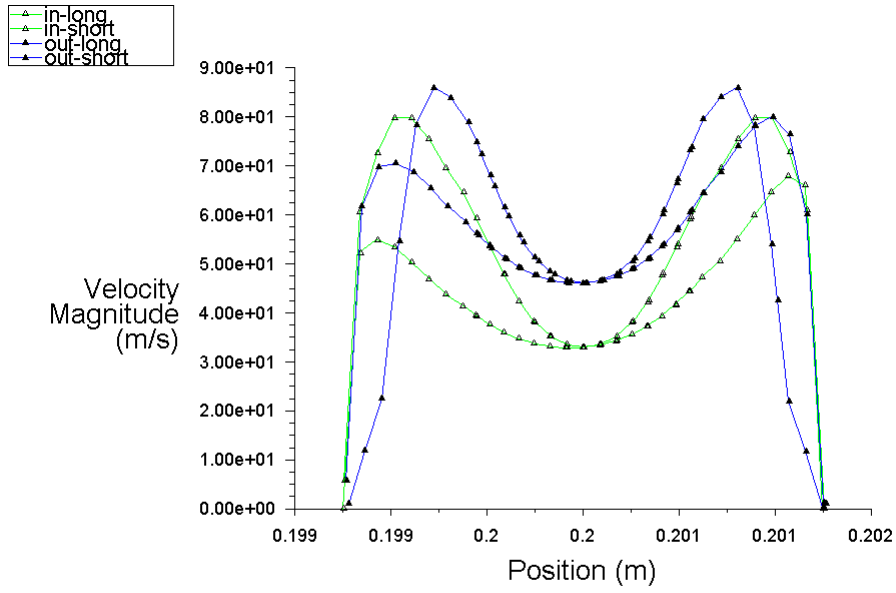


Velocity Magnitude (Time=4.3350e-03) Jul 14, 2015
 ANSYS Fluent 14.5 (3d, dp, pbns, ske, transient)

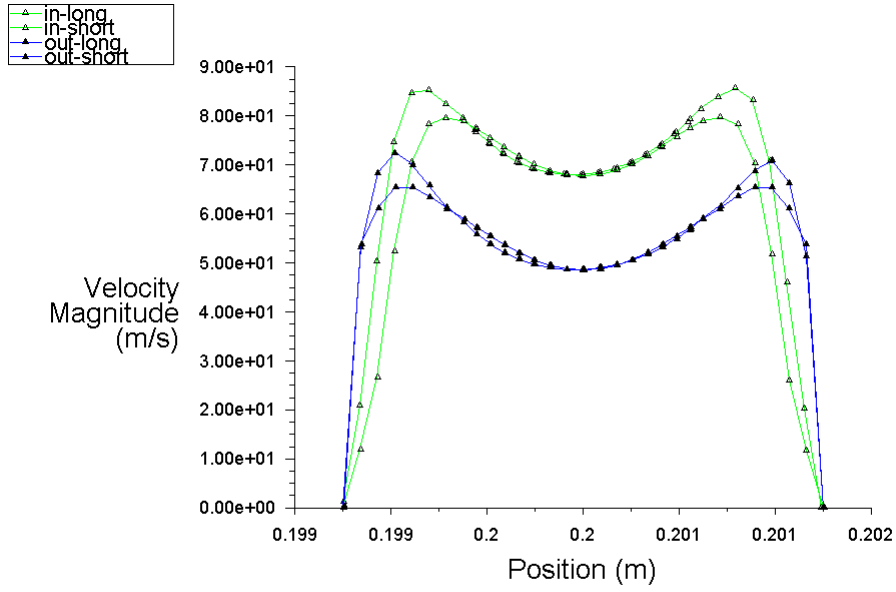


Velocity Magnitude (Time=4.6410e-03) Jul 14, 2015
 ANSYS Fluent 14.5 (3d, dp, pbns, ske, transient)

Figure 3.6.. *Model-R* velocity profiles $\{d_O, V_j\}, \{w_O, V_j\}$



Velocity Magnitude (Time=4.3350e-03) Jun 28, 2015
ANSYS Fluent 14.5 (3d, dp, pbns, ske, transient)



Velocity Magnitude (Time=4.6410e-03) Jun 28, 2015
ANSYS Fluent 14.5 (3d, dp, pbns, ske, transient)

Figure 3.7.. *Model-C* velocity profiles $\{d_o, V_j\}$

The velocity profiles are acquired at different locations of the orifice and slot, mainly along the length and width for the rectangular slot or the perpendicular diameters for the circle $\{d_O, w_O\}$ and also at the entrance and exit of the orifice or slot along h_N . These velocity profiles are taken during the 8th pressure cycle for approximate inflow and outflow temporal phases after 1445 and 1537 time steps. When the same ω_δ frequency is provided to both the models, having the same orifice and slot area A_O , it is noted that the circular orifice of *Model-C* has more velocity V_j coming out than the rectangular slot of *Model-R*. Velocity profiles undergo significant development along the orifice length h_N . It is observed that these velocity profiles depend on the local conditions.

4. Hot Wire Anemometry

To measure the velocity of the jet V_j from the actuator, Hot Wire Anemometry experimenting is used. The flow from the synthetic jet actuator is highly unsteady and also contains a region of high vorticity, requiring a large dynamic range to measure. For this chapter, the approach for making the velocity measurements for different operating frequencies ω_δ of the actuator is given. Most of the measurements of velocity require substantial amount of time to acquire results and the placement of the probe affects the velocities that are being measured. HWA presents interesting advantages to jet measurements, especially for investigating frequency response, as hot wires have a very high frequency response in the range of $10^4 - 10^5$ (TSI, 1993). Most of the operating range of the actuator in the current study operates between 20-4000 Hz. Therefore, it should not be difficult for the hot wire to capture this motion of the fluid.

4.1 Purpose

The purpose of these experiments is to obtain frequency response plots by measuring V_j peak velocities at various frequencies ω_δ and to compare them with the results obtained from the low fidelity analysis LEM tool.

4.2 Equipment

1. Hot wire probe, E_{HW}
2. *IFA 300* anemometer
3. RS232 interface
4. DAQ with *ThermalPro* software
5. Oscilloscope
6. Function generator, E_δ
7. Amplifier
8. *Model-C* SJA with single diaphragm and circular orifice
9. *Model-R* SJA with single diaphragm and rectangular slot
10. *Model-D* SJA with double diaphragm and circular orifice

4.3 Principles

A thin wire is mounted to supports and a surface area A_w of the wire is exposed to the changing velocity V_j emitting from the device. When the current I is passed through the wire, heat T_w is generated. At equilibrium, the velocity and the current must be balanced by T_s , the heat loss to surroundings.

$$I^2 R_w = h_T \cdot A_w (T_w - T_s) \quad (4.1)$$

Velocity changes are related to the convective heat transfer coefficient h_T . If the velocity changes then the balance of the relation changes too and the wire temperature T_w and current will change until it reaches a new equilibrium. For flows with non-constant temperature, the wire resistance R_w can also be modeled as a function of fluid temperature T_s .

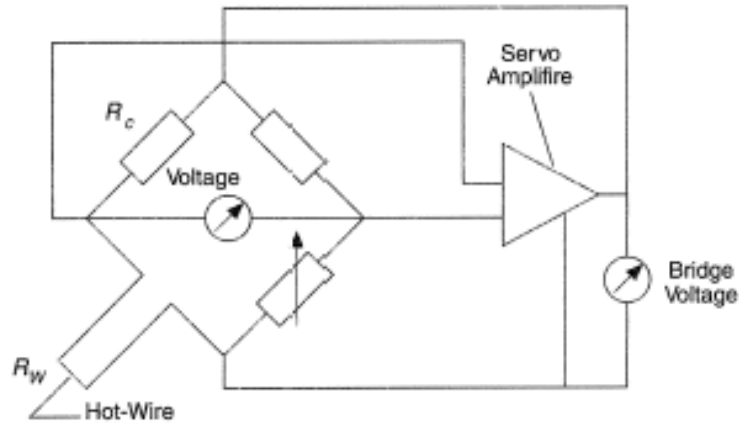


Figure 4.1.. Hot wire anemometer circuit

For constant-temperature hotwire anemometers, King's Law uses the following equation:

$$h_T = a + b\bar{V}_j^c = \frac{I^2 R_w}{A_w(T_w - T_s)} \quad (4.2)$$

Where $\{a, b, c\}$ are calibration constants, and V_j is the orifice velocity to be solved for. This is a form of a heat transfer equation for the heat loss from the sensor to the fluid. This fit gives a reasonable curve with only a few points.

The following assumptions are used for simplified static analysis:

- Velocity impacts normally on the wire of the probe uniformly over its entire length.
- Density and fluid temperature are constant.
- Radiation losses are small.
- Temperature is uniform over the length of the sensor.

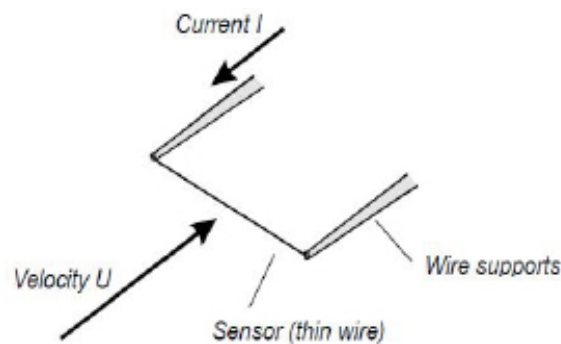


Figure 4.2.. Hot wire probe

4.4 Anemometer

A constant-temperature anemometer (*IFA 300*) is a bridge and amplifier circuit that controls a tiny wire and keeps the sensor resistance constant, as depicted in figure 4.1. Depending on the sensor used, it provides up to 300 kHz frequency response. For measuring fluid temperature, each module is designed with a built-in thermocouple circuit and for making temperature corrections. All operations, including setup, calibration, and data acquisition are software-controlled via an RS-232 interface. *IFA 300* anemometer and the interface board are shown below.

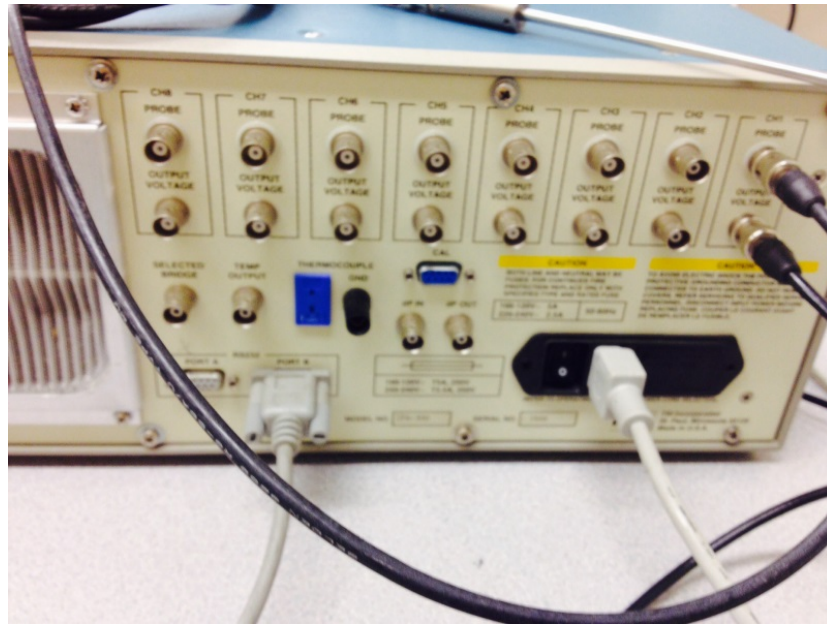


Figure 4.3.. Anemometer with *Channel 1* connection

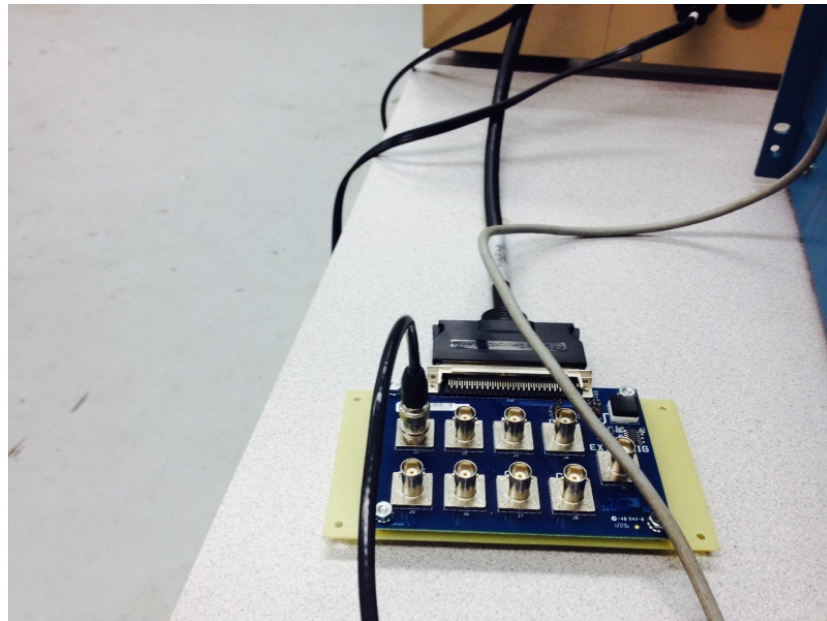


Figure 4.4.. HWA interface board

As a fluid flow passes over the heated hot wire probe, the amplifier senses an off-balance in the bridge. In order to keep the bridge balance, the current to the top of the bridge is adjusted. Built in software relates the velocity of the flow from the information obtained using King's Law as discussed in the previous section. The voltage measurement of the bridge is sensitive to temperature as well as velocity changes. The anemometer has a built-in thermocouple circuit that is attached to a thermocouple which measures the temperature of the fluid for constant-temperature calibration. Each *IFA 300* anemometer has eight channels with built-in signal conditioning.

4.5 Method

The input of *Channel 1* on the back of the *IFA 300* anemometer is connected to the probe. *Channel 1* output voltage E_{HW} is connected to the DAQ board, which is connected to the computer running *ThermalPro* software. The software allows control of the *IFA 300* anemometer and the A/D converter through the interface. The software allows the user to select the channels to be used and measures the resistance of the sensor. Options include setting the sampling rate for the A/D converter, making corrections for the temperature drift and the atmospheric pressure for the fluid, quantifying velocity data with flexible units, and entering probe position for plotting the data.

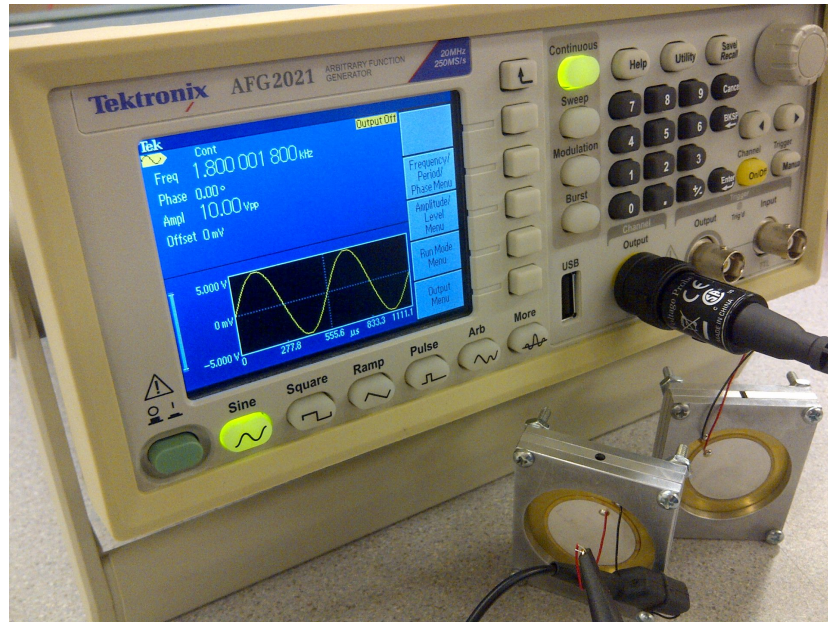


Figure 4.5.. Function generator E_δ with *Model-C* and *Model-R*

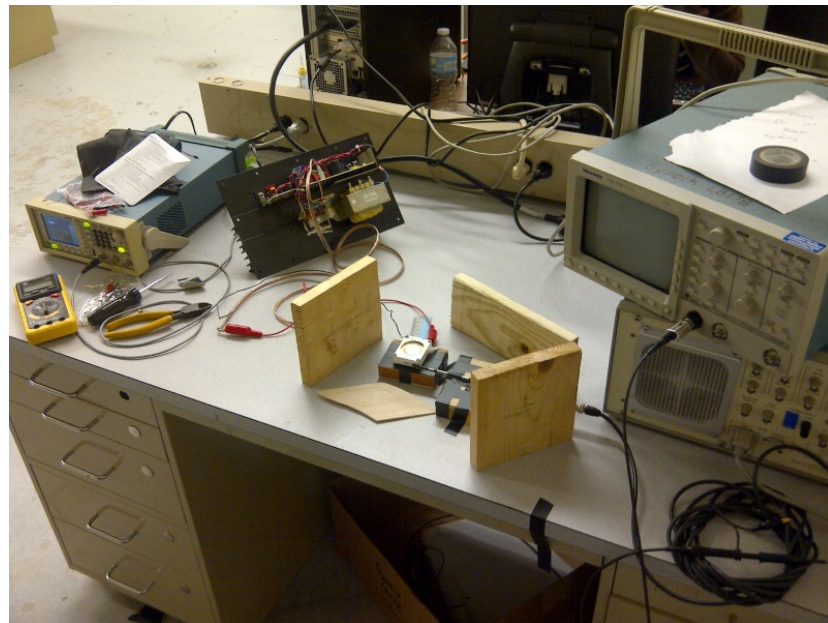


Figure 4.6.. Experimental setup with function generator, amplifier, SJA, hot wire probe, anemometer, DAQ board, and computer



Figure 4.7.. Hot wire probe and *Model-R* SJA with rectangular slot

The calibration program in the software allows calibration of the sensor probe using calibration files for the specified probe supplied by the manufacturer TSI.

Using the data acquisition program, each batch of data is displayed on a time history display. Temperature, mean velocity, and the turbulence intensity are also displayed. Data can be stored for further analysis.

The post processing program of the software allows calculation of the mean velocity, normal stress, turbulence intensity, skewness coefficient, etc and also displays the complete statistical results for different types of probes. The program also displays a histogram of the stored data and saves it via ASCII text file. This file can be used to plot the velocity data obtained.

4.6 Results

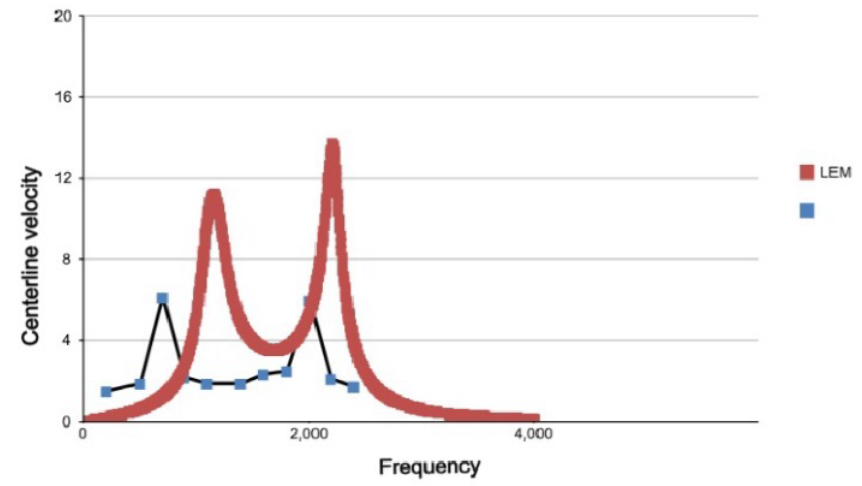


Figure 4.8.. Frequency response for *Model-C* LEM and HWA experiment $\{\omega_\delta, \bar{V}_j\}$

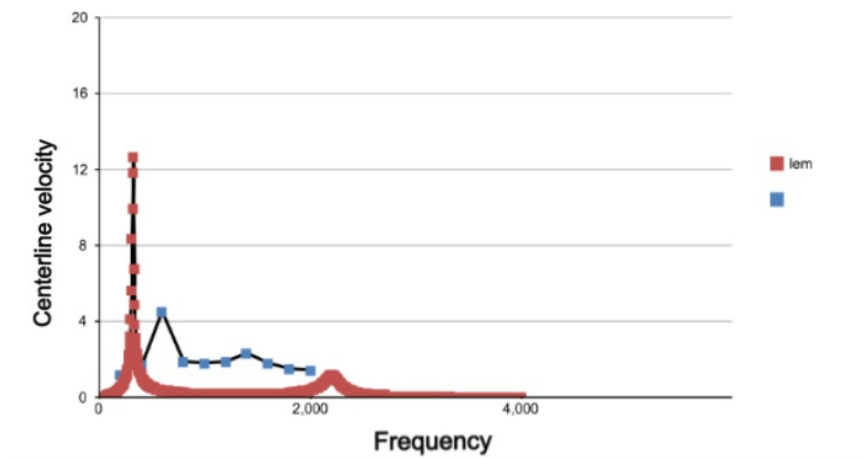


Figure 4.9.. Frequency response for *Model-R* LEM and HWA experiment $\{\omega_\delta, \bar{V}_j\}$

Frequency response of the actuators with the circular orifice and the rectangular slot are provided below and were validated against LEM low fidelity analysis results.

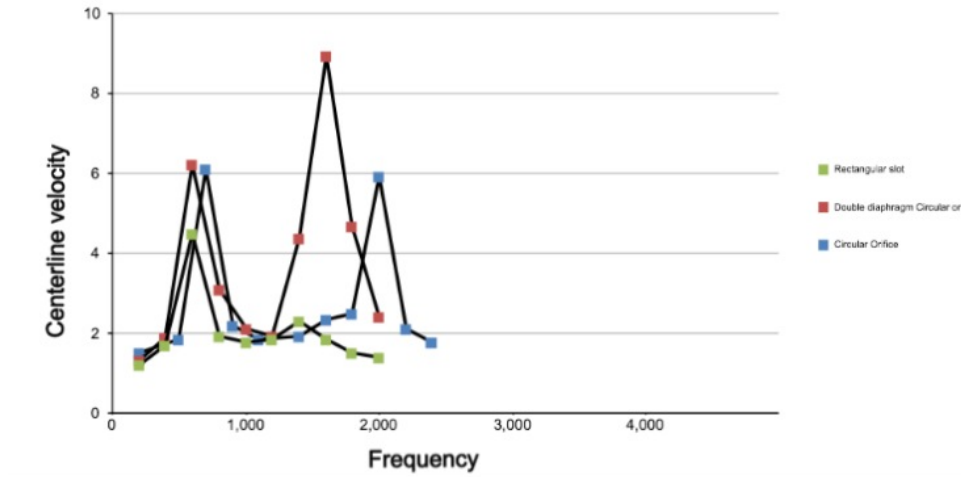


Figure 4.10.. Frequency response graph for actuators *Model -C, -R, and -D* $\{\omega_\delta, \bar{V}_j\}$

LEM has a set of limitations to be operated within. The shape effects are given priority, since the primary goal is to test the actuator on the modified wing as a control device.

Results from the hotwire experiment failed to agree with the LEM frequency response plot. However, in these cases LEM showed a similar number of peaks as in HWA experiments and the frequency ranges for the 1st peak and 2nd peak maximum velocities are almost similar to what was observed with experiments. For not fully developed flows, LEM results are overshooting if experimental results are considered accurate.

4.7 Alternate Model

For further comparison, the Gallas LEM is validated with another set of actuator geometrical parameters from (de Luca et al., 2000), where they developed a different LEM model and actuator design based on the basic laws of fluid dynamics similar to (Sharma, 2007)'s perspective. The three differential equations that describe these actuator dynamics are given by

$$\ddot{\delta} + 2\zeta_D\omega_D\dot{\delta} + \omega_D^2\delta = \omega_D^2\Delta\delta \sin\omega_\delta t - \frac{P_C A_D}{m_D} \quad (4.3)$$

$$\frac{V_C}{\gamma P_a} \frac{dP_C}{dt} - A_D\dot{\delta} = -A_O V_j \quad (4.4)$$

$$\ddot{V}_j + \frac{K_d}{h_N} |V_j| \dot{V}_j + \omega_H^2 V_j = \frac{A_D}{A_O} \omega_H^2 \delta \quad (4.5)$$

Derivation of the analytical model is described in (de Luca et al., 2000). This is the model that they used to predict performance and determine synthetic jet actuator geometrical parameters. By using these geometrical parameters in the Gallas LEM model and plotting the results with the experimental data from their research, a comparison can be made. First, in figure 4.11 a plot giving validation of their model with experimental results is given and then the comparison is made in figure 4.12. The parameters for their actuator design is given in tables 4.1 and 4.2.

Table 4.1.. Geometric parameters and properties of (de Luca et al., 2000) actuator

			Property
Orifice Diameter	d_O	(mm)	2
Orifice Height	h_N	(mm)	2
Cavity Diameter	d_C	(mm)	35
Cavity Width	w_C	(mm)	3
Voltage Applied	E_δ	(V)	35, 70

Table 4.2.. Piezoelectric diaphragm properties and dimensions (de Luca et al., 2000)

			Piezoceramic	Shim
Young's Modulus	E	(pa)	6.7×10^{10}	9.7×10^{10}
Poisson's Ratio	ν		0.31	0.36
Density	ρ	(kg/m^3)	8000	8490
Thickness	t_D	(mm)	0.23	0.4
Diameter	d_D	(mm)	23	35

The plots in figure 4.11 below show the frequency response plots from this different LEM model with experimental results at two different E_δ voltages of 35 and 70 V for the same geometrical parameters.

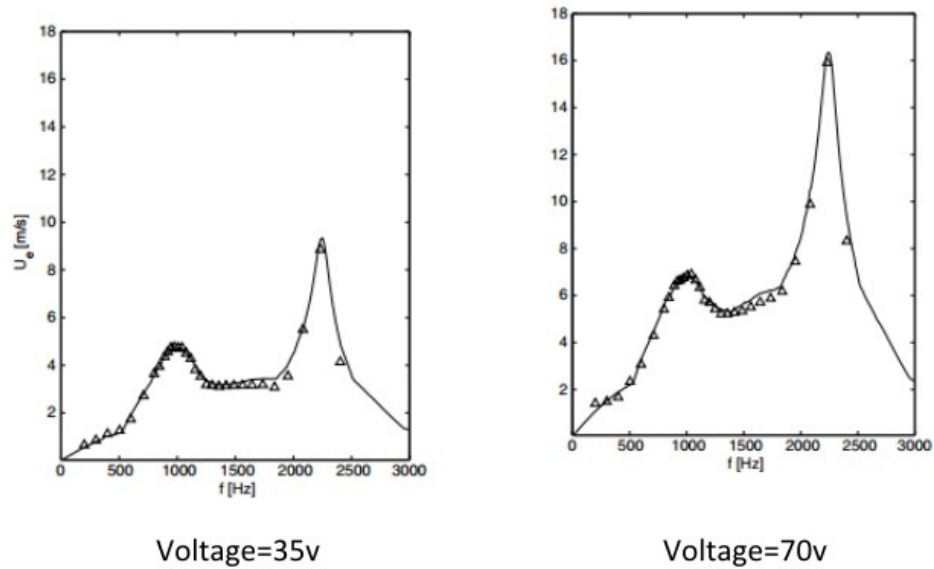


Figure 4.11.. Numerical-experimental comparison of average exit flow velocity frequency response $\{\omega_\delta, \overline{V}_j\}$, (de Luca et al., 2000)

Triangles represent the experimental measurements, black curves indicate results from the numerical solution. After having looked at the difference in the frequency response plots between the LEM and HWA experimental results in the current thesis, the Gallas LEM is once again validated with geometric parameters of this actuator design given, derived from an alternate method.

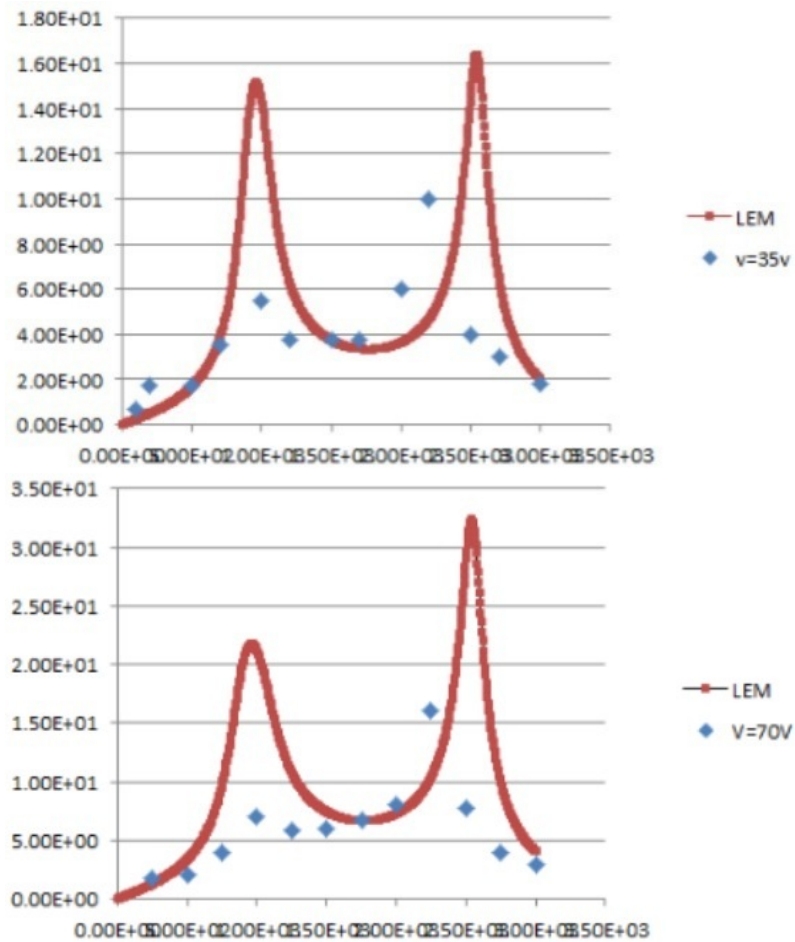


Figure 4.12.. Experimental validation of actuator developed using LEM model based on Sharma's work vs Gallas LEM model using (de Luca et al., 2000) actuator design $\{\omega_\delta, V_j\}$

When using the equal actuator parameters, the current Gallas model of the LEM used in this project overshoots the experimental results by a factor of 2–3 times from the (de Luca et al., 2000) results. This is observed for both of the cases with 35 V and 70 V. Similar type of differences in results are obtained from the comparison of the Gallas LEM with the prototype HWA experimental results in this thesis, indicating a scalar overshooting correlation.

5. Wind Tunnel Experiment

For the final part of the project, the actuator model was placed inside the wing section. In this chapter an overview of the wind tunnel experiments is provided. The modified Glauert wing section is mounted inside the subsonic wind tunnel and forces are obtained with and without the SJA actuation. From the obtained forces, coefficients of lift C_L (dimensionless parameter) were obtained based on the free stream flow conditions V_∞ and the wing section geometry. These are compared with the theoretical C_L of a 2D airfoil.

5.1 Modified Glauert Airfoil

The shape of the airfoil is different from many other conventionally used airfoils in aviation. Separated flow can be observed, this is due to the discontinuity bump near the trailing edge. This phenomenon can be used to understand the synthetic jet actuator flow physics when embedded into the airfoil. Dimensioning of the wing is given in the below table:

Table 5.1.. Modified Glauert wing dimensions

Wing Span	b_w	(cm)	12.4
Airfoil Chord	c_w	(cm)	14
Surface Area	s_w	(cm^2)	16×12.4
Slot Position	x_{TE}	(cm)	$0.7c_w$

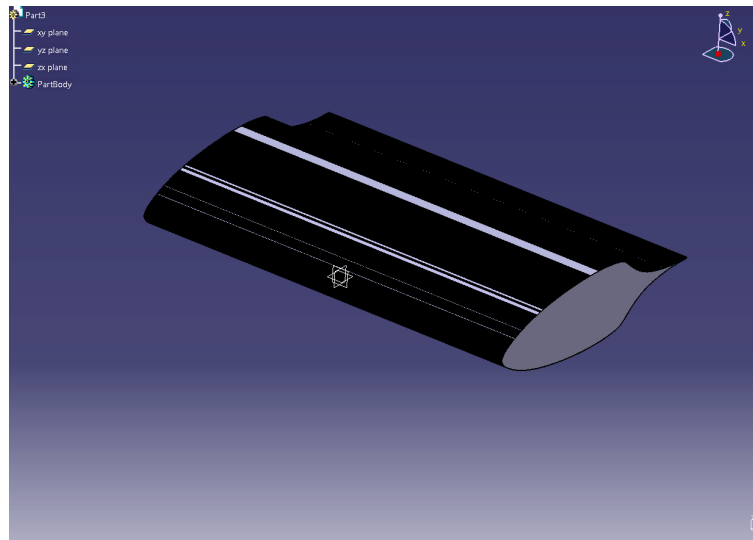


Figure 5.1.. Modified Glauert airfoil

With a 14 cm chord c_w and a span of 12.5 cm b_w , the actuator was embedded at a ratio of 0.7 of the chord. This is considered the optimal location to increase the enhancement of the flow, as the value was obtained from a parallel research project.

The Embry-Riddle Aeronautical University subsonic wind tunnel is used in this experiment. Voltages E_{WT} were obtained from every run of WT through a data acquisition computer using *LabView Express* software. Post processing needs to be carried out in order to compare the lift curve plots.

5.2 Strain Gauge Principle

When a force is applied to the spindle, it causes a bending moment at each point along the length of the internal beams. The bending moment stretches one surface and compresses the opposite surface of the beam. There is a fine wire which is woven

back and forth across the surface of the beam, causing an increase in resistance when the wire is stretched along with the beam surface. When a force F is applied, the resistance of the wire increases and the current drops. Unknown forces can be obtained by measuring the current change ΔE_{WT} and then comparing the current change with the calibration data to find out what the unknown force was to produce that result. Lift component of the balance has been calibrated by placing the weights directly on the force balance platform. The setup used for lift component calibration is shown in figure 5.2.

5.3 Calibration

A strain gauge balance system verifies the accuracy of the system by applying known loads and noting the resultant voltages. When known loads are applied, voltages can be recorded on a digital voltmeter. Recorded data is plotted as output voltages versus applied load and a straight line is fitted to the data. Calculating the slope of the straight line gives the calibration constant with units of Volts output per unit of force applied. The output voltages are simply multiplied by the calibration constants to determine the aerodynamic forces.



Figure 5.2.. Lift component calibration

Weight Tare To get only the lift produced by the wing mounted inside the wind tunnel, weight tare needs to be carried out to subtract the additional lift. Additional lift might be added to the wing due to free stream flow conditions when the wind tunnel is at rest. To test this, the wind tunnel needs to be turned off and measurements need to be recorded from the DAQ computer.

5.4 Operation of Wind Tunnel

After checking weight tare, the wing section needs to be mounted and secured properly into the AEROLAB Pyramidal Strain Gauge Balance System. The deviation blades accelerate the airflow into the wind tunnel when it is operated. The desired velocity range V_∞ can be set for the experiments.

As already mentioned output from the WT can be recorded for different AoA or α in terms of voltages E_{WT} . For obtaining more steady and constant velocity flows, the fan should be allowed to run for a few seconds to stabilize internal wind tunnel conditions.

To convert the voltages E_{WT} in terms of physical values of force, the calibration constants $\{a, b\}$ are used, which are the voltage-lift curve slope and the offset values that had been measured and given by $a = 0.732$ and $b = -0.243$. Using the below equation, force L can be calculated.

$$E_{WT} = aL + b \quad (5.1)$$

Similarly L_e or excess lift from the wind tunnel, as already discussed, is subtracted from the obtained lift force L to get the final lift L_f .

$$L_f = L - L_e = 0.5\rho V_\infty^2 s_w C_L \quad (5.2)$$

The coefficient of lift is obtained by rearranging formula 5.2. Similar calculations give the drag coefficient.

$$C_L = \frac{2L_f}{\rho V_\infty^2 s_w} \quad (5.3)$$

$$C_D = \frac{2D_f}{\rho V_\infty^2 s_w} \quad (5.4)$$

Theoretical coefficient of pitching moments can also be obtained:

$$C_M \approx -\frac{C_L}{4} \quad (5.5)$$

The setup of the experiment has been provided below. Function generation and amplification E_δ is used to generate the signal for the actuator.

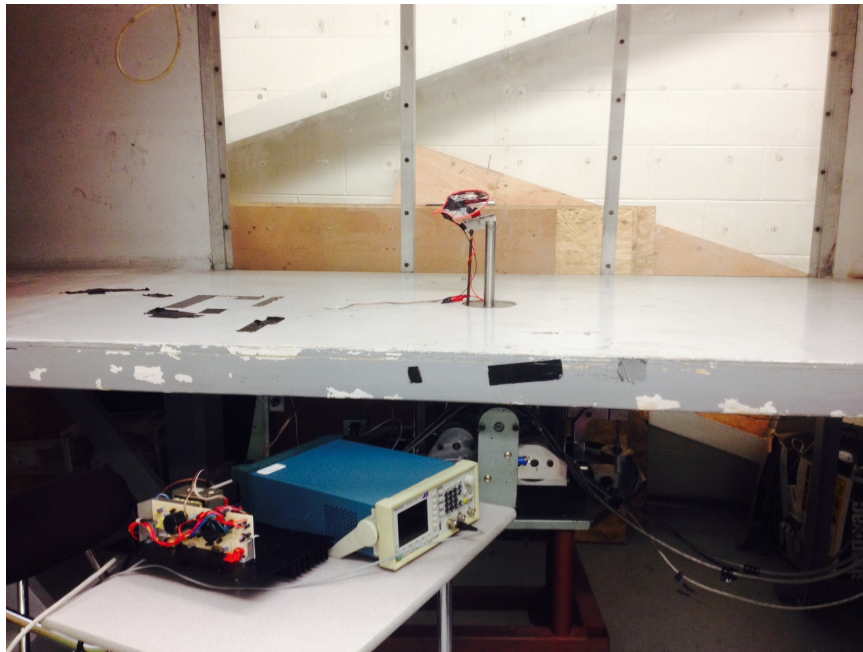


Figure 5.3.. Wind tunnel with actuator setup



Figure 5.4.. Experimental setup of the wing

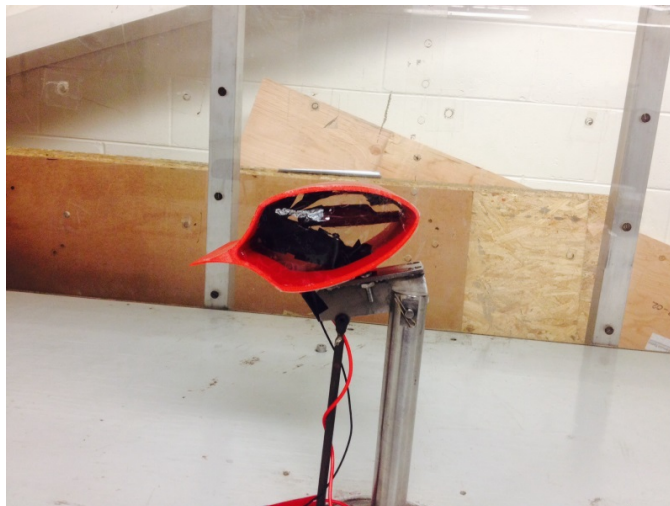


Figure 5.5.. Experimental setup of the wing with actuator embedded

5.5 Results

Coefficients plotted against α graphs show the curves, one with the actuator turned on and the other is a clean case without any actuator. The associated Reynolds numbers for the experiments are 38000 and 76000 for the 5 and 10 m/s cases based on the airfoil chord.

Double diaphragm SJA with circular orifice, *Model-D*, was used because it has more \bar{V}_j velocity than *Model-C* and *Model-R*, around 9 m/s . Plots below show the lift curves that were plotted for two different WT V_∞ velocities, 5 m/s and 10 m/s .

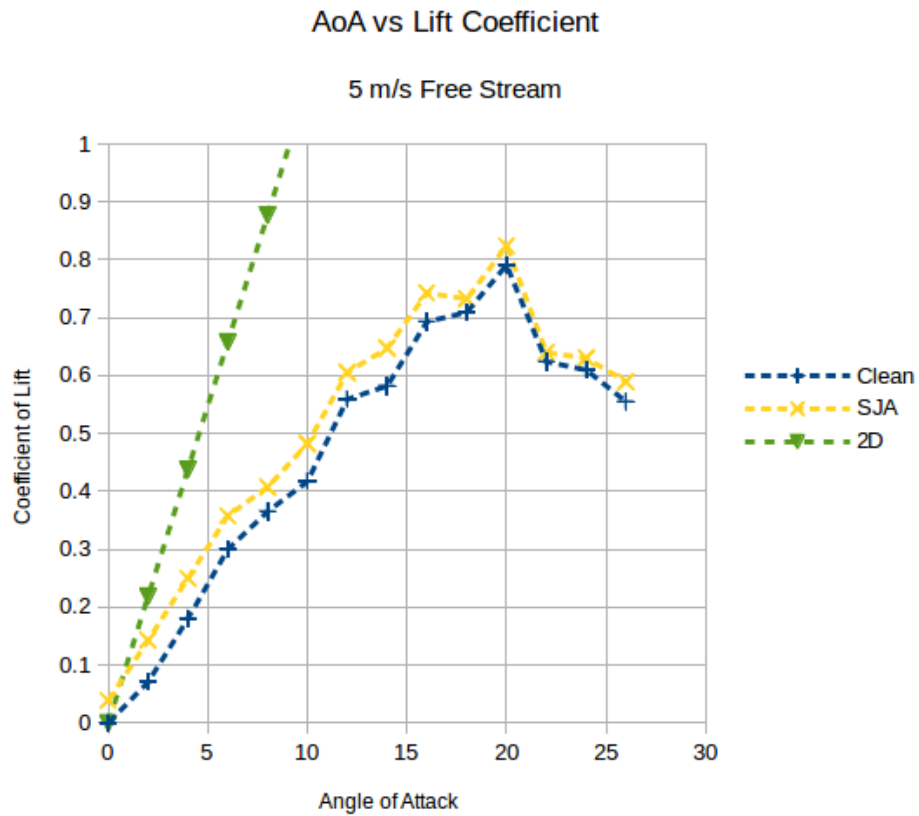


Figure 5.6.. Lift curve plot for clean and SJA case at 5 m/s $\{\alpha, C_L\}$

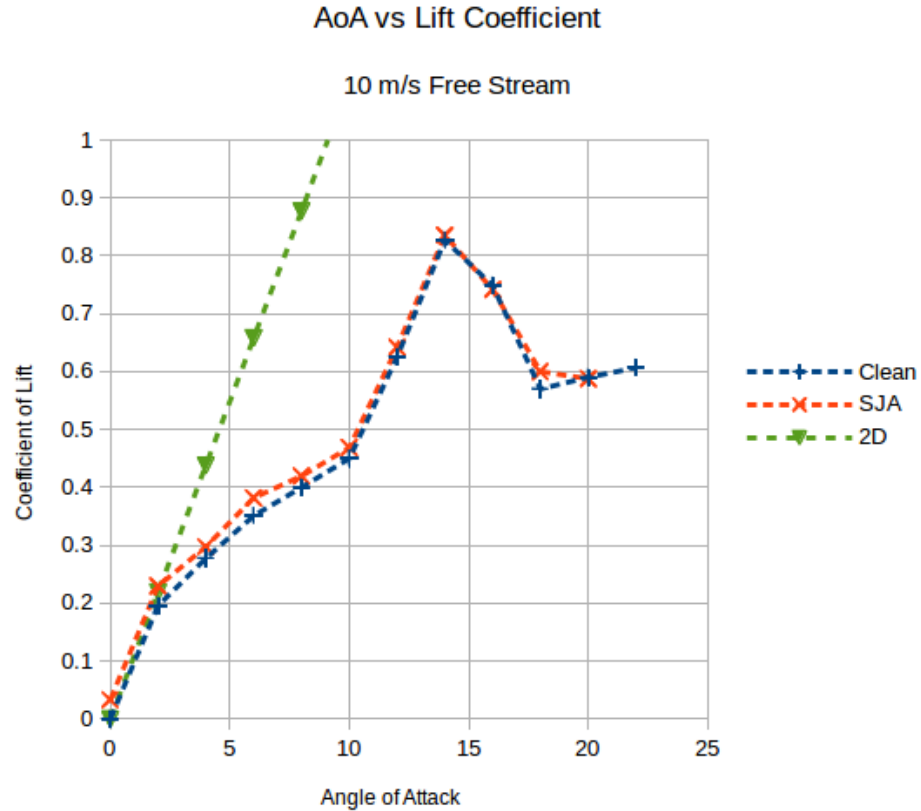


Figure 5.7.. Lift curve plot for clean and SJA case at 10 m/s $\{\alpha, C_L\}$

The typical value for lift curve slope with a 2D airfoil is around $2\pi\alpha$ (about 0.11 per degree). It implies that for each 1 degree of change in the airfoil angle of attack, the lift coefficient will be increased by 0.11. Thin airfoil theory addresses an airfoil with almost zero thickness and infinite wingspan. As the thickness to chord ratio increases, C_L moves away from the theoretical value. From the graphs, for free stream velocity of 5 m/s , the actuation case showed an increase in C_L of 8% and decrease in C_D of 5% over the clean case. For free stream velocity at 10 m/s , there is a change in $\{C_L, C_D\}$ of approximately $\{5\%, 3\%\}$.

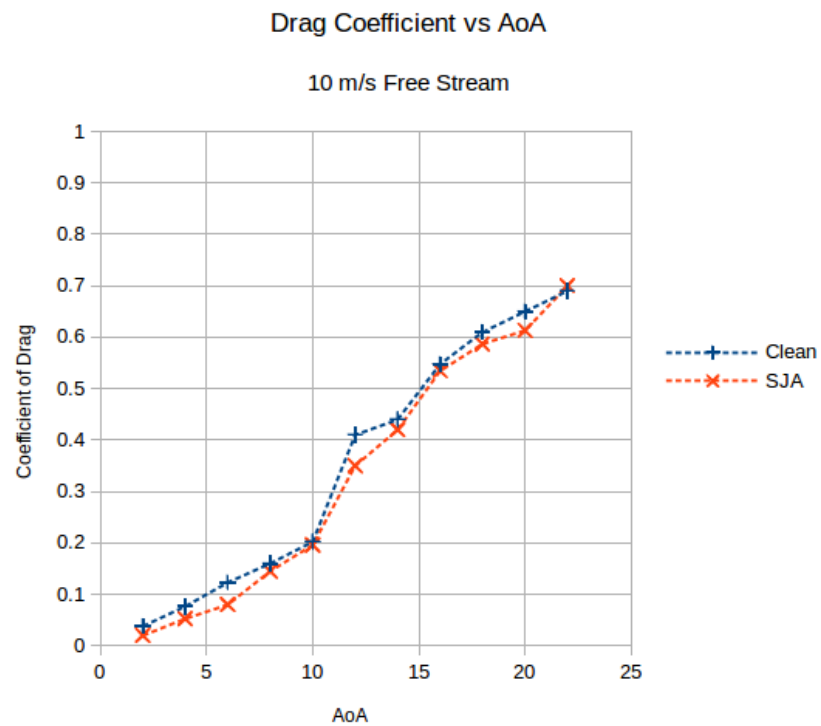
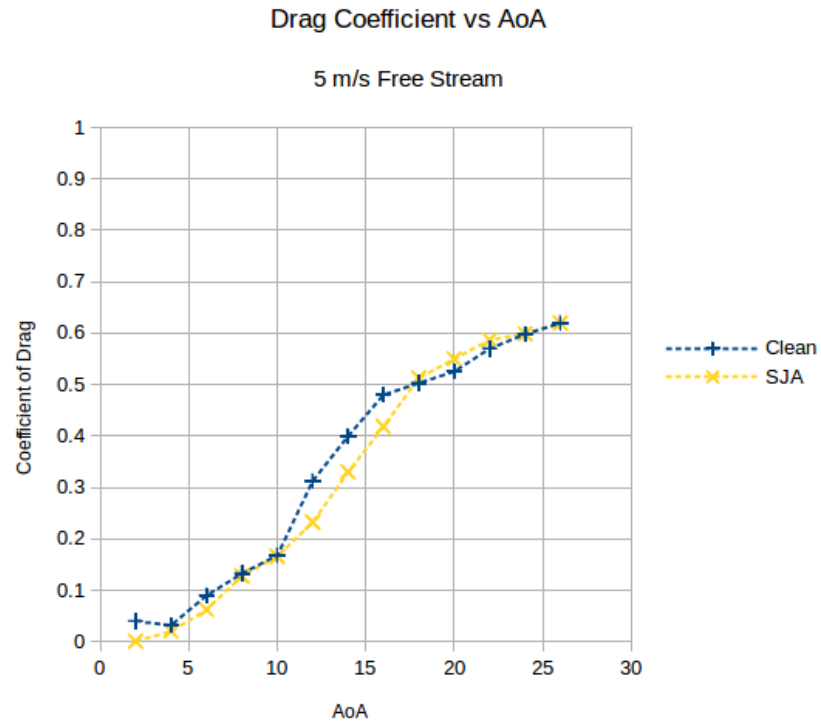


Figure 5.8.. Drag curve plots for clean and SJA case $\{\alpha, C_D\}$

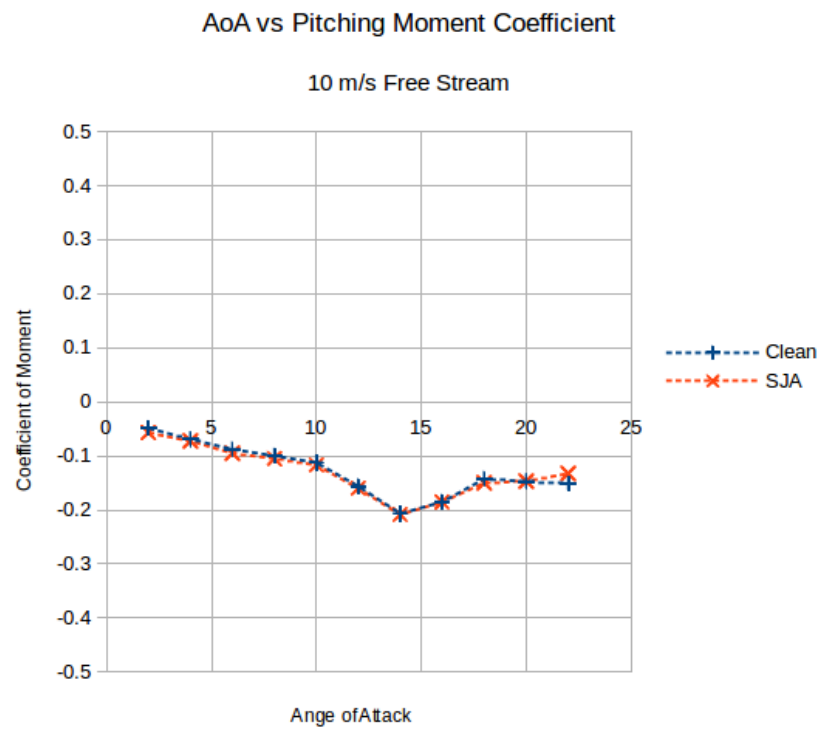
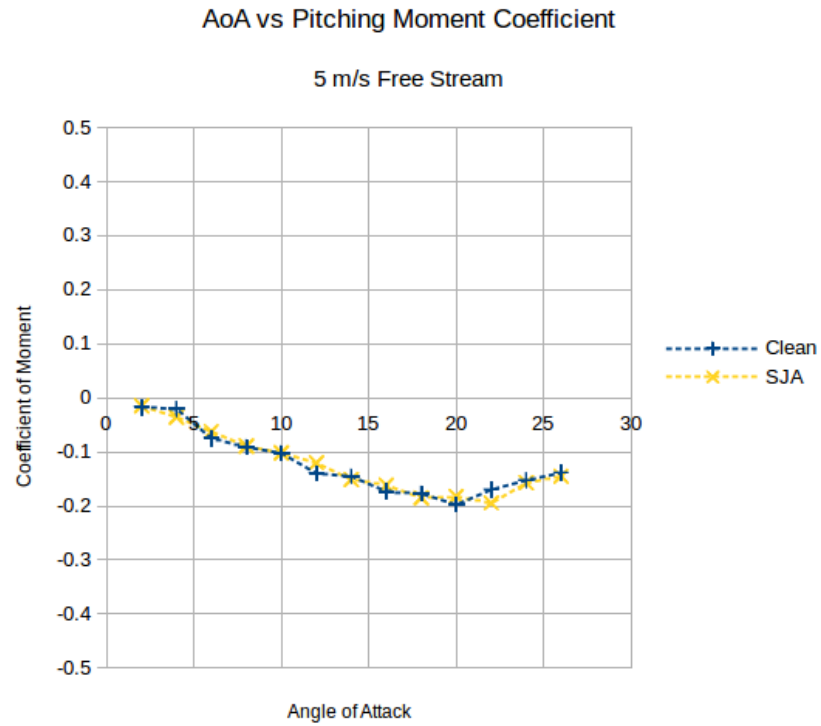


Figure 5.9.. Moment curve plots for clean and SJA case $\{\alpha, C_M\}$

6. Conclusions

Due to increasing usage and uniqueness of their behavior, Synthetic Jet Actuators stand out from various other active and passive flow control techniques. Designing an actuator is a function of geometrical parameters, operational parameters, and flow conditions on the actuator-wing unit. All the possible parameters affect the design and the performance of the synthetic jet actuator. Advancement in computational science helps to understand some of the parameters, but trying to incorporate all of the parameters into a single computational study requires large amounts of numerical data and is also very time consuming.

Due to large parameter space involved in the design of the actuator, low dimensional models are important to establish design optimization conditions. DI - Dynamic Incompressible flow model, SC - Static Compressible model and LEM - Lumped Element Model (Tang et al., 2007), (Gallas, Holman, & Cattafesta, 2005) are examples.

Circular orifice and rectangular slot prototypes had been developed using LEM and validated using Hot Wire Anemometer experiments, additionally their differing velocity profiles due to shape effects were obtained using 3D CFD simulations. It is to be noted that the placement and length of the hot wire probe affect the output of the frequency response measured. Because results from the LEM didn't show good agreement with HWA experimental results, the Gallas LEM is also validated with (de

Luca et al., 2000) and it is found that the present LEM model used in this study is overshooting the V_j peak velocities.

Finally wind tunnel experiments were conducted and lift curve slopes with and without actuator placement were plotted. The effect noticed in both the cases is not very outstanding but hopeful. This might be due to the ineffective performance of the actuator. The design of the actuator needs to be optimized and understood better before proceeding further into research. Only a single actuator was placed in the wing section; however, embedding multiple actuators into the wing section might have significant additive effect on the desired characteristics.

Precise machining of materials used for the actuator is needed in order to reduce the weight and to improve the performance and cavity resonance characteristics. LEM is only capable of measuring first modes of the diaphragm frequency ω_D due to the λ_δ assumptions from the LEM. Thus, there is not much preliminary design operating information beyond the first mode of the diaphragm frequency. An effective diaphragm is also required, especially having effective piezoelectric-material to shim diameter and thickness $\{d_D, t_D\}$ ratios.

Due to limitations of the current research regarding design optimization analysis tools and immediately available materials, only a basic model of the actuator was developed. More research is recommended to develop mathematical models using reduced order methods that take more actuator configurations into consideration. Building on these tools will help in simulating and exploring parametric spaces for actuators and reactive flight control systems for Active Flow Control on a small UAV.

REFERENCES

- Bewley, T. (1999). New frontiers for control in fluid mechanics: A renaissance approach. *3rd Joint Fluids Engineering Conference*.
- Bourlier, A. (2010). *Investigation of scaling effects of synthetic jet actuators using high and low fidelity analyses* (Master of Science Thesis).
- Carpenter, P., & Lockerby, D. (2004). Modeling and design of microjet actuators. *AIAA Journal Vol. 42*.
- Cattafesta, L., & Sheplak, M. (2011). Actuators for active control. *Annual Review of Fluid Mechanics*.
- de Luca, L., Girfoglio, M., & Coppola, G. (2000). Modeling and experimental validation of the frequency response of synthetic jet actuators. *AIAA*.
- Gad-El-Hak, M. (2000). *Flow control: Passive, active, and reactive flow management*. Cambridge.
- Gallas, Q. (2002). *Lumped element modeling of piezoelectric-driven synthetic jet actuators for active flow control* (Master of Science Thesis).
- Gallas, Q., Holman, R., & Cattafesta, L. (2005). Design tools for zero-net-mass-flux separation control devices. *University of Florida*.
- Gallas, Q., Sheplak, M., & Cattafesta, L. (2005). Design optimization tool for synthetic jet actuators using lumped element modelling. *Final Report for NAG-1-03031*.
- Glezer, A., & Amitay, M. (2002). Synthetic jets. *Annual Review of Fluid Mechanics*.
- Golmes, L., Crowther, W., & Wood, N. (2006). Towards a practical piezoceramic diaphragm based synthetic jet actuator for high subsonic applications-effect of chamber and orifice depth on actuator peak velocity. *3rd AIAA Flow Control Conference*.
- Golubev, V., & Mankbadi, R. (2009). Modeling of acoustic streaming for micro air vehicle propulsion and flow control. *AIAA*.
- Golubev, V., Mankbadi, R., & Nakhla, H. (2009). Towards complete mav control using arrays of synthetic jets: Preliminary study. *NSF Grant*.
- Holman, R. (2006). *An experimental investigation of flows from zero-net mass-flux actuators* (Master of Science Thesis).
- James, R., Jacobs, J., & Glezer, A. (1996). A round turbulent jet produced by an oscillating diaphragm. *Physics of Fluids*.

- Kral, L. (2000). Active flow control technology. *ASME Fluids Engineering Division Brief*.
- Mane, P., Mossi, K., Rostami, A., Bryant, R., & Castro, N. (2007). Piezoelectric actuators as synthetic jets: Cavity dimension effects. *Journal of Intelligent Material Systems and Structures*.
- McCormick, D. (2000). Boundary layer separation with directed synthetic jets. *38th Aerospace Sciences Meeting and Exhibit*.
- Mohseni, K., & Mittal, R. (2014). *Synthetic jets: Fundamentals and applications*. CRC Press.
- Moin, P., & Bewley, T. (1994). Feedback control of turbulence. *Applied Mechanics Review Vol. 47*.
- Rathnasingham, R., & Breuer, K. (1997). Coupled fluid-structural characteristics of actuators for flow control. *AIAA*.
- Sefcovic, J., & Smith, D. (2010). Proportional aerodynamic control of a swept divergent trailing edge wing using synthetic jets. *AIAA*.
- Seifert, A., & Pack, L. (1999). Oscillatory control of separation at high reynolds numbers. *AIAA*.
- Sharma, R. (2007). Fluid-dynamics-based analytical model for synthetic jet actuation. *AIAA*.
- Smith, B., & Glezer, A. (1997). Vectoring and small-scale motions effected in free shear flows using synthetic jet actuators. *35th Aerospace Sciences Meeting and Exhibit, AIAA*.
- Tang, H., Zhong, S., Jabbal, M., Garcillan, L., Guo, F., Wood, N., & Warsop, C. (2007). Towards the design of synthetic jet actuators for full-scale flight conditions. *Flow, Turbulence and Combustion*.
- TSI. (1993). Fluid mechanics constant temperature anemometer system. *Operational Manual*.
- Ugrina, S., & Flatau, A. (2004). Investigation of synthetic jet actuator design parameters. *Smart Structures and Materials*.